




# Airglow and Aurora in the Martian Atmosphere: Contributions by the Mars Express and ExoMars TGO Missions

Francisco González-Galindo<sup>1</sup>  · Jean-Claude Gérard<sup>2</sup> · Lauriane Soret<sup>2</sup> · Jean-Yves Chaufray<sup>3</sup> · Anna Fedorova<sup>4</sup> · Mats Holmstrom<sup>5</sup> · Franck Lefèvre<sup>3</sup> · Miguel Ángel López-Valverde<sup>1</sup> · Franck Montmessin<sup>3</sup>

Received: 31 July 2023 / Accepted: 8 May 2024 / Published online: 30 May 2024  
© The Author(s) 2024

## Abstract

The study of atmospheric emissions from orbit to probe the middle and upper atmosphere of Mars, which started with the Mariner missions, is living a golden era thanks to the European Space Agency (ESA) Mars Express mission and other subsequent missions built upon its success, including the ESA ExoMars Trace Gas Orbiter (TGO) mission. Here we summarize the most relevant information obtained by the analysis of atmospheric emissions data from Mars Express and TGO, about the temperature and density structure, the atmospheric dynamics, the chemistry and the atmospheric escape to space. Mars Express also opened a new field of research on Mars with the discovery of aurorae on the planet. We present here the most outstanding results collected by Mars Express about aurorae. Finally, we also discuss how later measurements by other missions have complemented Mars Express and TGO results, and the potential future developments relevant to this field of research.

**Keywords** Mars Express · Airglow · Aurora · ExoMars TGO · Dayglow · Nightglow

## 1 Introduction

Airglow and aurora are non-thermal atmospheric emissions that differ in the origin of their energy source. Airglow is ultimately produced by the interaction of solar radiation with the atmosphere, either by the direct effects of solar photons or by excitation by photoelectrons originated in photoionizations. Auroral emissions, on their side, have their origin in the collisions with the atmosphere of extra-atmospheric energetic particles (ions, electrons and neutrals).

Airglow, traditionally divided into dayglow and nightglow, is mostly observed in the ultraviolet (UV) and visible but also in the infrared (IR). It has been used since the beginning of the space age to obtain information about the upper atmospheres of the terrestrial planets. A list of the physical mechanisms resulting in airglow emission and of some of the most prominent emission systems in the UV can be found in Leblanc et al. (2006a) and Bougher et al. (2017).

In the IR, CO<sub>2</sub> and other atmospheric species like CO, ozone or water vapor sometimes present prominent non-thermal emissions produced by enhanced or depleted populations of

their vibrational states. At the low atmospheric pressures found at high altitudes, those state populations are not dictated by the local temperature but by other processes, in a situation known as non-Local Thermodynamic Equilibrium (non-LTE in what follows). The non-LTE processes include cascading from absorption of solar radiation, efficient emission to space, energy transfer during collisions with other species or isotopes which have non-thermal populations, or quenching. The vibrational excitation can later be relaxed as IR airglow emission, or can be thermalized via molecular collisions, both mechanisms playing a major role in the thermal balance of the upper atmosphere. A comprehensive review about non-LTE processes and their importance in the atmospheres of the terrestrial planets can be found in López-Puertas and Taylor (2001).

The UV dayglow of Mars was first observed by the Mariner 6, 7, and 9 NASA missions and the Soviet Mars 2 and 3 missions, and these observations allowed deriving values for the temperature at the exobase of Mars (Stewart et al. 1972) or setting upper limits for the abundance of oxygen in the upper atmosphere (Strickland et al. 1973). Among the features detected by these observations are the H Lyman- $\alpha$  emission, oxygen and carbon emission lines, the fourth positive and Cameron bands of CO and the UV doublet (VVD) and Fox-Duffendack-Barker (FDB) bands of CO<sub>2</sub><sup>+</sup> (Fox 1992). The Martian UV dayglow was also observed from observatories in Earth orbit such as the Hubble Space Telescope (Krasnopolsky et al. 1998) or the Far Ultraviolet Spectroscopic Explorer (FUSE) (Krasnopolsky and Feldman 2002), providing for example estimations of the abundance of Ar.

The visible and IR dayglow of Mars has also been observed from ground-based telescopes (e.g. Noxon et al. (1976), Deming et al. (1983), Krasnopolsky (2003) and references therein) and by the Infrared Space Observatory (ISO) satellite (Lellouch et al. 2000), but measurements of IR atmospheric emissions were rare before the advent of Mars Express. On the other hand, despite some attempts and their positive detection on Venus, no nightglow emissions from Mars could be detected before the arrival of Mars Express, which can be explained by the small size of Mars and its small nightside as seen from Earth making nightglow detections much more difficult at Mars than at Venus. Reviews of Mars airglow observations prior to Mars Express can be found in Fox (1992) and Bougher et al. (2017).

While observations of Mars airglow existed well before the arrival of Mars Express, the Martian aurora was discovered thanks to Mars Express observations, which is one of the highlights of the whole mission.

Regarding the European missions Mars Express (MEx) and ExoMars Trace Gas Orbiter (TGO), observations of airglow and aurora involve five MEx instruments, namely SPectroscopy for the Investigation of the Characteristics of the Atmosphere of Mars (SPICAM), Planetary Fourier Spectrometer (PFS), Observatoire pour la Mineralogie, l'Eau, les Glaces et l'Activite (OMEGA), Analyser of Space Plasmas and Energetic Atoms (ASPERA-3) and Mars Advanced Radar for Subsurface and Ionosphere Sounding (MARSIS), and the UV and visible spectrometer (UVIS) channel of the Nadir and Occultation for Mars Discovery (NOMAD) instrument on TGO. Detailed descriptions of these instruments and their observational strategies are presented in Wilson et al. (2024), this collection. A review of results from the first 10 years of operation of SPICAM, including airglow and aurora, can be found in Montmessin et al. (2017).

In the rest of this chapter, we will summarize the main discoveries by MEx and TGO about the airglow, with a focus on the physical information that can be derived from it, in Sects. 2 for the dayside emissions and 3 for the nightside emissions. The discovery of auroral emissions by Mars Express and its consequences will be described in Sect. 4. Subsequent related observations by later missions such as Mars Atmosphere and Volatile Evolution (MAVEN) and Emirates Mars Mission (EMM) will be reviewed in Sect. 5, and we will finish with a short summary and a discussion on future observations in Sect. 6.

## 2 Dayglow

Figure 1 shows average airglow spectra measured by Mars Express instruments in the UV and the IR spectral ranges, including the identification of different emission features. Most of the dayside emissions, such as the Cameron bands ( $\text{CO } a^1\Pi - X^1\Sigma^+$ ), the  $\text{CO}_2^+$  UV doublet (UVD,  $\text{CO}_2^+ B^2\Sigma^+ - X^2\Pi$ ), the CO fourth-positive bands ( $\text{CO } A^1\Pi - X^1\Sigma^+$ ) (Fig. 1, top left) or the different bands in the  $\text{CO}_2$  NIR spectrum around  $4.3 \mu\text{m}$  (Fig. 1 bottom), are ultimately produced by the interaction of solar radiation with the main constituent of Mars atmosphere,  $\text{CO}_2$ . This is also the case for the recently discovered in Mars O green and red lines in the visible spectral range. As such, these emissions provide information on the atmospheric density and, through the analysis of their scale height (the rate of variation with altitude), the atmospheric temperature can be derived. Measurements of these emissions originating from  $\text{CO}_2$  are described in Sect. 2.1. This and other methods to study the temperature of the Martian atmosphere are discussed thoroughly in Giuranna et al. (2024), this collection.

Dayglow emissions not directly related to  $\text{CO}_2$  are the H Lyman- $\alpha$  emission, the O emission at 130.4 and 135.6 nm, the  $\text{O}_2$  dayglow and the  $\text{N}_2$  Vegard-Kaplan bands. The H Lyman-alpha and the O 130.4 nm emission are produced by resonant scattering of solar photons and provide information on the H density and O density in the exosphere, and thus on the rate of water escape to space. Similarly, the O 135.6 nm emission is due to photoelectron impact on atomic oxygen. More details about the water cycle and its escape can be found in Montmessin et al. (2024), this collection. The NO and the  $\text{O}_2$  nightglow are produced by the recombination of atoms produced in the dayside by photodissociation and transported to the nightside, so these emissions trace the atmospheric dynamics. The  $\text{O}_2$  dayglow originates in ozone photodissociation, providing information on ozone abundance. Similarly, the  $\text{N}_2$  Vegard-Kaplan bands inform about the  $\text{N}_2$  abundance. More details about the chemistry and composition of the Martian atmosphere can be found in Vandaele et al. (2024), this collection.

### 2.1 Probing the Temperature/Density Structure

#### 2.1.1 $\text{CO}_2$ UV Emissions

Two of the most prominent UV emission systems in Mars dayglow are the CO Cameron bands (170–270 nm) and the  $\text{CO}_2^+$  UVD ( $\sim 289$  nm) (Fig. 1, panel a). The first emission arises from the de-excitation of CO from the  $a^3\Pi$  excited level to the ground state. The  $\text{CO } a^3\Pi$  level is populated mainly by  $\text{CO}_2$  photodissociation and photoelectron dissociative impact,  $\text{CO}_2^+$  dissociative recombination and electron impact on CO. The UVD originates in the de-excitation of  $\text{CO}_2^+$  ( $B^2\Sigma^+$ ) state, which is populated by  $\text{CO}_2$  photoionization, photoelectron impact and fluorescent scattering. If the contribution of CO electron impact for the Cameron bands and the fluorescent scattering for UVD can be neglected, then the emission in both systems will be proportional to the  $\text{CO}_2$  density, and the scale height of the emission can be assimilated to the  $\text{CO}_2$  scale height and used to derive atmospheric temperatures. This method was already used to derive thermospheric temperatures from Mariner measurements (Stewart et al. 1972).

This same approach was used to derive temperatures in the upper atmosphere from SPICAM-UV dayglow observations. Leblanc et al. (2006a) derived temperatures at altitudes between 170 and 190 km from a set of 45 limb observations obtained between October 2004 and March 2005. The derived temperatures showed no clear variation with Solar Zenith Angle (SZA), season, latitude or longitude, which was in part attributed to the small size of

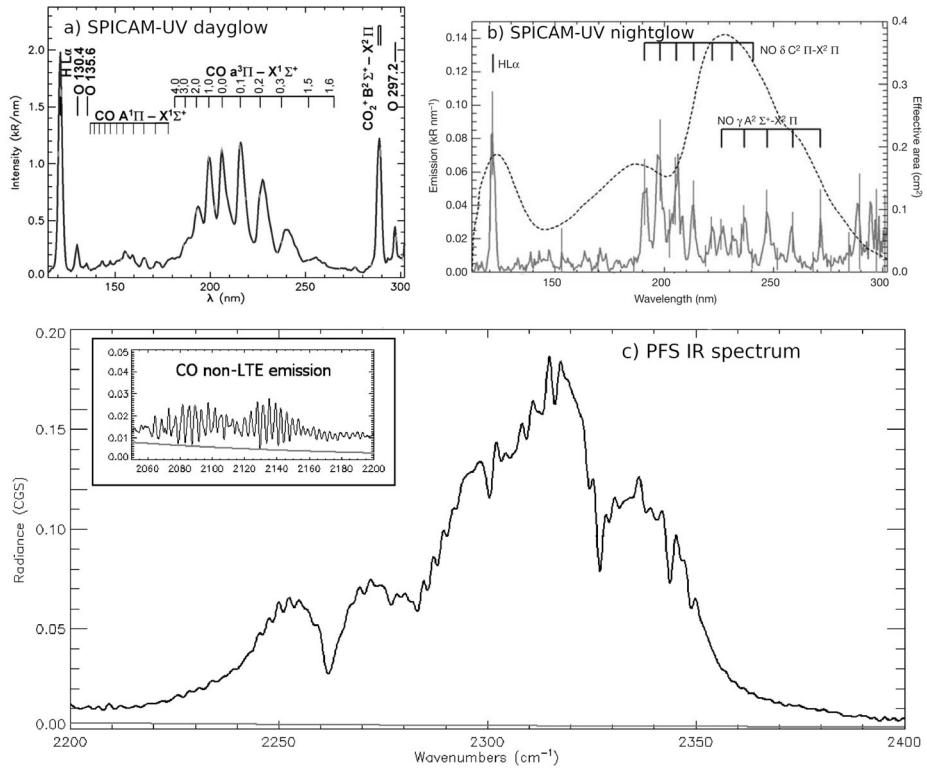


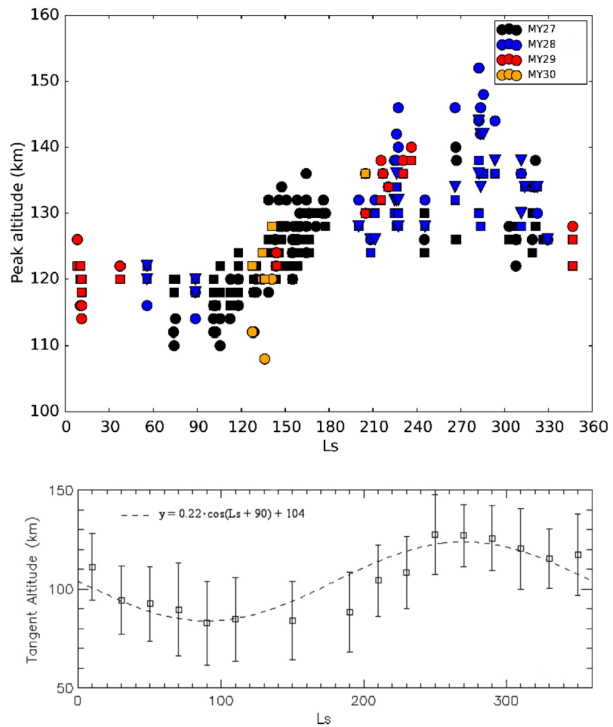
**Fig. 1** Average spectra in the UV measured by SPICAM-UV in the dayside (panel a)) and the nightside (panel b)) adapted from Leblanc et al. (2006a) and Bertaux et al. (2005b), respectively. Panel c): average IR spectrum of CO<sub>2</sub> and CO (inset) emissions measured by PFS, adapted from Giuranna et al. (2018). The dashed line in panel b) represents the SPICAM UV detector efficiency. Adapted with permission, copyright by the American Geophysical Union (a)), Nature Publishing Group (b)) and Elsevier Inc. (c))

the sample. The average temperatures derived were  $252 \pm 13$  K for the Cameron bands and  $201 \pm 10$  K for UVD. The difference in the derived temperatures was attributed to the contribution of CO<sub>2</sub><sup>+</sup> dissociative recombination to the Cameron bands.

However, a later theoretical work, using a Global Climate Model, showed instead that, contrary to what was assumed before, the CO electron impact excitation could have a non-negligible contribution to the Cameron bands, introducing a bias towards large values when the scale height of the Cameron bands is used to derive temperatures (González-Galindo et al. 2021). Leblanc et al. (2006a) also found elevated temperatures derived from the Cameron bands in their only observation obtained above a crustal field region, which they tentatively attributed to the effect of hot electrons increasing the contribution of electron impact dissociative excitation.

A later analysis of the SPICAM-UV dataset obtained during the whole lifetime of the instrument confirmed the lack of dependency of the derived temperatures with the solar activity, SZA, or geographical location (Stiepen et al. 2015a). A strong temperature variability was found, ranging between 180 and 400 K with an average value of 275 K for the Cameron bands, and between 150 and 400 K with an average value of 270 K for the UVD. The anal-

**Fig. 2** Top: Seasonal variation of the SPICAM-UV measured peak altitude of the Cameron bands (circles with different colors indicating measurements obtained at different Mars Years), compared to LMD-MGCM simulations for different Mars Years (squares and triangles). Adapted from González-Galindo et al. (2018). Bottom: Seasonal variation of the PFS measured altitude of the CO<sub>2</sub> 4.3 μm emission, adapted from Giuranna et al. (2018). L<sub>s</sub> = 0 corresponds to the Northern spring equinox, L<sub>s</sub> = 90 to the Northern summer solstice, and L<sub>s</sub> = 270 to the Northern winter solstice. Aphelion occurs at L<sub>s</sub> = 71 and perihelion at L<sub>s</sub> = 251. Reproduced with permission, copyright by AGU (top) and Elsevier Inc. (bottom)



ysis of the whole dataset also ruled out the potential effects of crustal fields over the derived temperatures.

Beside the derivation of temperatures from their scale heights, the peak altitude of these two emission systems is correlated to the atmospheric density structure and can thus inform about variations in the CO<sub>2</sub> density. Similarly, the variation of the peak intensities should depend on the intensity of the incoming solar radiation. Leblanc et al. (2006a) hinted a potential seasonal variation in the peak altitudes, confirmed by later analysis (Cox et al. 2010; González-Galindo et al. 2018) and caused by the variations of thermospheric CO<sub>2</sub> density due to the eccentricity of the Martian orbit (Fig. 2). The analysis of the data obtained during the Mars Year (MY) 28 global dust storm showed an increase in the observed peak altitude (González-Galindo et al. 2018), confirming that the effects of global dust storms propagate to the thermosphere. The peak intensities were found to decrease with increasing SZA and to increase with solar activity, in agreement with theoretical expectations (Cox et al. 2010).

SPICAM-UV observations of these two emission systems has also motivated the development of different computational models, either 1-D (Shematovich et al. 2008; Cox et al. 2010; Jain and Bhardwaj 2012) or 3D (González-Galindo et al. 2018) to interpret the observations. Most of these models show that a reduction in the cross section of CO<sub>2</sub> and CO electron impact is needed to reproduce the observed intensity of the Cameron bands. Recent laboratory measurements of these cross sections already confirm a strong reduction of these cross sections over the previously used values (Lee et al. 2021, 2022). Their impact on the ability of computational models to reproduce airglow measurements still needs to be evaluated.

Finally, Soret et al. (2023) analyzed the UV dayglow measured by the UVIS channel of NOMAD. They statistically analyzed the CO Cameron and the CO<sub>2</sub><sup>+</sup> UVD emissions and concluded that these emissions occur at ~122.5 km. They also detected the full wavelength range of the CO<sub>2</sub><sup>+</sup> FDB band system for the first time since the Mariner missions. They found that this emission is produced at ~70% by photoionization of CO<sub>2</sub> (which populates the shorter wavelengths of the spectrum) and ~30% by resonance scattering of solar radiation.

### 2.1.2 CO<sub>2</sub> IR Emissions

The CO<sub>2</sub> non-LTE emission at 4.3 μm (see Fig. 1) is a common feature to the atmospheres of the Earth, Venus, and Mars, playing an important role in the heating balance of their upper atmospheres (López-Puertas and Taylor 2001; López-Valverde et al. 2011). Given its dependence on the CO<sub>2</sub> density structure, it is possible to use this emission to derive CO<sub>2</sub> density profiles, though the subtleties of the interplay between radiative transfer and non-LTE relaxation processes make some practical implementations difficult unless a good description of the thermal structure is also available (Jiménez-Monferrer et al. 2021).

On Mars, the first observations of these emissions came from the ISO satellite (Lellouch et al. 2000), and the first measurements from Martian orbit were obtained by the PFS instrument on Mars Express (Formisano et al. 2005b) and later by OMEGA (Piccialli et al. 2016). PFS provides measurements with a relatively high spectral resolution but a large field of view (and thus a relatively poor vertical resolution), while OMEGA measurements present low spectral resolution, but good vertical resolution, so that the measurements from both instruments are complementary.

The first nadir and limb PFS measurements of this emission system allowed validating a non-LTE model and identifying the main bands contributing to the emission and its altitude variation (López-Valverde et al. 2005; Formisano et al. 2006). In particular, in the nadir pointing, a strong contribution from the second hot bands was found with maximum emission coming from the region between 80 and 120 km above the surface (López-Valverde et al. 2005). In the limb geometry, a contribution to the emission from minor CO<sub>2</sub> isotopes, significantly larger than that expected from their abundances, was also identified (Formisano et al. 2006), and well reproduced with simulations by López-Valverde et al. (2011).

Systematic analysis of the data accumulated by PFS and OMEGA during several Martian years of operation (Piccialli et al. 2016; Giuranna et al. 2018) showed common features in both datasets: the peak of the emission is located at an approximate common pressure level, and the altitude and intensity of the emission display a prominent seasonal variation similar to that found in the CO<sub>2</sub> UV emissions (Fig. 2), with minimum values around the aphelion season and maximum values close to the perihelion season. This seasonal variation was attributed to the contraction/inflation cycle in the lower atmosphere due to the eccentricity of the Martian orbit. The shape of the spectra changes also with altitude and with SZA, revealing changes in the contribution of different bands at different altitudes, imposing strong constraints on non-LTE models. A strong decrease of the emission with increasing SZA is also found. For a given season, maximum emission is found around the subsolar point due to the strong dependence of the solar pumping mechanism on the intensity of the solar radiation. A morning-evening asymmetry in the emission is also found in the PFS dataset, attributed to differences in the morning and evening temperature structure.

Jiménez-Monferrer et al. (2021) adapted a non-LTE retrieval scheme used for the Earth atmosphere to Martian conditions and applied it to 3 OMEGA limb observations, allowing derivation of CO<sub>2</sub> density profiles above 120 km. Temperature profiles were derived from hydrostatic equilibrium. Significant differences with a Global Climate Model used as a-priori for the retrieval scheme was found, in particular for the temperatures. A systematic

application of this (or other) retrieval scheme to the whole OMEGA and PFS datasets is still to be done, and could provide interesting information about the density and temperature variations in the thermosphere.

### 2.1.3 O 297.2 nm/Green/Red Lines

These emissions originate mainly from CO<sub>2</sub> photodissociation populating excited O levels, namely the O(<sup>1</sup>S) level for the 297.2 nm and the green line, and the O(<sup>1</sup>D) level for the red line, and the subsequent de-excitation to lower levels. Note however that other processes, such as electron impact excitation or cascading from upper levels, can also contribute to populate these excited levels.

The SPICAM instrument did not cover the visible part of the spectrum but the presence of the [OI] 297.2 nm trans-auroral forbidden emission in the dayglow (Barth et al. 1971, 1972; Leblanc et al. 2006a; Cox et al. 2010) and aurora (Soret et al. 2016) anticipated that the green line at 557.7 nm might be also observable by an instrument with a spectral coverage extending into the visible. The two transitions have a common upper level so that their intensity ratio is equal to the ratio of their transition probabilities, which favors the green line.

SPICAM observations of the 297.2 nm dayglow indicated that its maximum brightness at limb between 100 and 150 km tangent height was less than 1 kR (Leblanc et al. 2006a; Cox et al. 2010). However, the SPICAM sensitivity at the longest wavelengths rapidly drops (see panel b of Fig. 1), which made it difficult to provide absolute intensities.

These measurements stimulated interest for a tentative detection of the OI green line. A special mode of observation orienting the nadir UVIS/NOMAD channel to the sunlit limb led to the discovery of the presence of the OI green line (Gérard et al. 2020). Two limb scans (ingress and egress) between about 50 and 200 km separated by about 45 degrees of latitude were collected in the ‘inertial limb’ mode when the line of sight was fixed in the inertial space. In addition, spectral observations were also performed in the ‘limb tracking’ mode when the UVIS line of sight was constrained to remain at a nearly fixed tangent altitude above the surface. A clear signature of the 557.7 nm emission was observed in the dayglow with double intensity peaks of over 200 kR near 80 and 120 km (Fig. 3). The lower one corresponds to the production of O(<sup>1</sup>S) from CO<sub>2</sub> photodissociation by solar Lyman- $\alpha$  radiation while the upper one is caused by the CO<sub>2</sub> photodissociation by extreme ultraviolet solar radiation.

The weaker [OI] 297.2 nm emission was also observed from UVIS/NOMAD. Measurements of both oxygen lines have made it possible to determine a ratio  $\sim 16.5$  between the visible and ultraviolet emissions, in agreement with ab initio calculations. This is a factor of 2 larger than terrestrial airglow and auroral determinations.

Further analysis of one Martian year of UVIS limb observations by Soret et al. (2022) has confirmed this ratio and shown that both the peak altitude and the intensity of both oxygen emissions exhibit seasonal variations in response to the variations in insolation and changes in the thermal structure along Mars’ orbit, roughly consistent with those found in the CO<sub>2</sub> UV and IR emissions (Fig. 2) and in the ionosphere (Peter et al. 2024), this collection.

Aoki et al. (2022) developed an inversion method to determine daytime density and retrieve temperature in the upper mesosphere and lower thermosphere from the OI 557.7 nm dayglow limb profiles. They retrieved the CO<sub>2</sub> density between 90 and 140 km and the temperature near 80 km from the limb measurements. The method was based on a combination of a Bayesian inversion algorithm of the limb profiles with predictions of the O(<sup>1</sup>S) volume emission rate from the one-dimensional Photochemical Airglow Mars (PAM) model (Gkouvelis et al. 2018). The temperature retrieval was based on the temperature dependence of the

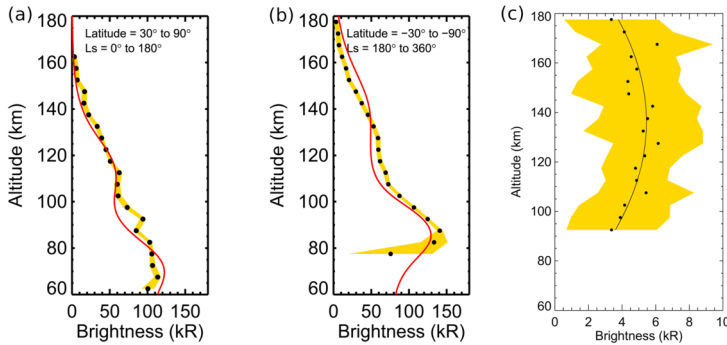
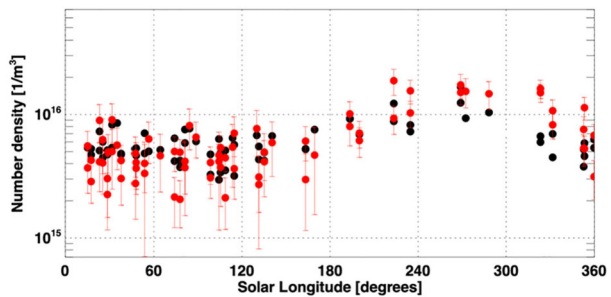


**Fig. 3** (a and b) Average limb profiles of the 557.7 nm dayglow emission measured with NOMAD-UVIS during two different periods. Note the seasonal change in the altitude of the peak emission; (c) average of 4278 limb profile of the 630 nm dayglow. The yellow zone indicates the 1- $\sigma$  uncertainties on the brightness and the black curve is a second order fit to the data. Adapted with permission from Soret et al. (2022), copyright by AGU

**Fig. 4** Seasonal variation of the CO<sub>2</sub> density at 140 km (red dots). The black dots indicate the densities predicted by the MCD that were used as a priori values in the retrieval process. Reproduced with permission from Aoki et al. (2022), copyright by AGU



quenching coefficient of  $O(^1S)$  by CO<sub>2</sub>. The densities show a large seasonal variation both around 90 and 140 km and reach maximum values in the vicinity of perihelion as shown in Fig. 4. This is a consequence of the temperature variation in the lower atmosphere driven by the dust content and the distance from the Sun. The temperatures around 80 km exceed the values predicted by the Mars Climate Database (MCD). This feature is consistent with the warm atmospheric layer in nighttime.

The oxygen red line at 630 nm associated with the  $O(^1D)$  to  $O(^3P)$  transition was later observed with a brightness about 20 times lower than the green line (Gérard et al. 2021). The production rate of the  $O(^1D)$  state by Lyman-alpha photons exceeds that of  $O(^1S)$ , but the radiative lifetime of the  $O(^1D)$  atoms is about 150 times longer. Since the quenching coefficients by CO<sub>2</sub> have similar values, collisional deactivation is by far more efficient for the red line, resulting in a lower brightness and a different, broader, altitude distribution, as shown in Fig. 3 (see also Fig. 3 in Gérard et al. (2021)). Soret et al. (2022) identified the second component of the doublet at 636.4 nm about 3 times weaker than the 630 nm component, in agreement with the ratio of the transition probabilities.

Comparison with the PAM photochemical model indicated that dayglow emissions are well predicted by current photochemistry and showed that  $O(^1D)$  is populated by CO<sub>2</sub> photodissociation in the mesosphere but mainly from photoelectron impact on O and the decay from  $O(^1S)$  at thermospheric altitudes, diffculting the use of this line to obtain information on CO<sub>2</sub>. Simultaneous observations of the green (and UV 297.2 nm) and red dayglow



provide information on variations in the thermosphere in response to seasonal changes, perturbations by solar events and tropospheric dust storms (Gkouvelis et al. 2020). Soret et al. (2023) found a ratio of 15.8 between the oxygen green and UV lines.

## 2.2 Probing Atmospheric Escape

To escape from a planet, a species needs to have an energy larger than the escape energy and keep it during its travel away from the planet. For this reason, the escape processes are sensitive to the conditions of the upper atmosphere (thermosphere and exosphere) where the collisions become rare (Chassefière and Leblanc 2004; Johnson et al. 2008). On Mars, for light species like atomic hydrogen, the temperature of the upper atmosphere is sufficient to allow a small fraction to have an energy larger than the escape energy. This process is called thermal escape (or Jeans escape) because it is directly controlled by the temperature of the upper atmosphere.

For heavier species such as helium, carbon, oxygen, nitrogen and argon on Mars, thermal escape is not efficient but other processes called non-thermal processes can produce atoms with an energy larger than the escape energy. For atomic oxygen, one well studied process is the dissociative recombination of the  $O_2^+$  ions with an electron (McElroy 1972). Also, the solar wind can interact with the Martian upper atmosphere and transfer a part of its energy to the main species leading to increase the atmospheric escape. For H this process is much less efficient than the Jeans escape. However, this escape, under ion form, is generally easier to measure directly (Barabash et al. 2007). Ion escape rates measured by ASPERA-3 are discussed in Barabash et al. (2024), this collection.

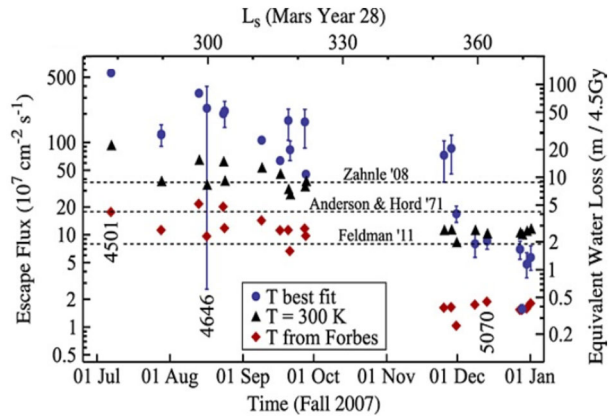
### 2.2.1 H Lyman-Alpha

Jeans escape of H is difficult to observe directly, but the hydrogen atoms, gravitationally bounded to Mars, form an extended exosphere that can be observed through the resonant scattering of the solar Lyman-alpha photons at 121.6 nm (Anderson and Hord 1971). The observation of this emission at limb can then provide information on the vertical distribution and the amount of hydrogen in the Martian upper atmosphere and on the expected fraction of escaping atoms. This information is used to derive the escape flux of hydrogen using the Jeans formula (Chaufray et al. 2008) by assuming a value for the exospheric temperature, which can introduce a significant uncertainty in the calculation.

The first observations of the Martian hydrogen corona at 121.6 nm were acquired during the Mariner 6, 7 and 9 missions (Anderson and Hord 1971; Anderson 1974). Because the emission is optically thick, the direct derivation of H density from the emission profile is difficult. Instead, a forward comparison between the observations and the simulated intensity calculated from a parameterized hydrogen density model, coupled to a radiative transfer model, is required.

This method was applied to interpret the first 6 limb observations done by SPICAM on an altitude range extending from 400 km to 4000 km (Chaufray et al. 2008). SPICAM observations showed two different brightness profiles at SZA  $\sim 30^\circ$  and  $90^\circ$ : the brightness is almost constant between 400 and 1000 km and decrease above 1000 km at SZA  $\sim 30^\circ$ , while the brightness decreases monotonically from 400 km at SZA  $\sim 90^\circ$ . The parameterized 1D profile of atomic hydrogen was calculated using a diffusion model from 80 to 200 km (exobase altitude), based on Krasnopolsky and Feldman (2002), and an exospheric model (Chamberlain 1963) without satellite particles above the exobase. The brightness profile was simulated for a set of values of the two free parameters of the model (hydrogen density and

**Fig. 5** Temporal variability of the H escape rate derived from SPICAM UV observations of the H corona, during the last part of MY28. The different symbols represent results using different assumptions for the exobase temperature. Adapted with permission from Chaffin et al. (2014), copyright by AGU



temperature at the exobase) and the best fit used to deduce the parameters. The profiles at SZA  $\sim 30^\circ$  were difficult to reproduce with the nominal calibration and a single hydrogen population. However, with a modification of the calibration by  $\sim 20\%$  they could be fitted with a single population, and the shapes of the profiles at SZA  $\sim 30^\circ$  and  $90^\circ$  were consistent with those expected for an optically thick emission.

A larger set of observations was studied showing large seasonal variations of the brightness and the derived hydrogen escape rate with a peak near the Martian southern solstice summer during the dusty season of the Martian year 28 (Chaffin et al. 2014) (Fig. 5). These results were consistent with the Hubble Space Telescope observations of the Martian hydrogen corona obtain at the same time in support of the Mars Express observations (Clarke et al. 2014).

These variations were unexpected because they were in contradiction with the classical paradigm of hydrogen escape, in which the source of thermospheric hydrogen was dominated by the chemical reaction between the long-living molecular hydrogen, produced ultimately by water photodissociation in the lower atmosphere, and ions in the thermosphere. However, this increase in hydrogen escape was found to be correlated with large seasonal variations of the water vapor abundance measured in the Martian mesosphere (Maltagliati et al. 2013), unveiling that the dissociation of water vapor in the mesosphere was essential to explain the hydrogen variations in the thermosphere and its escape rate (Chaffin et al. 2017). Mars Express observations were thus fundamental in changing the paradigm of water escape from Mars. More details about the driving mechanisms of this variation are discussed in Montmessin et al. (2024), this collection.

SPICAM observations during the Martian years 28 and 29 were compared to the simulated brightness obtained using the 3D hydrogen abundance in the Martian thermosphere, calculated with the LMD-MGCM (Forget et al. 1999; González-Galindo et al. 2009) and extended into the exosphere using a kinetic approach (Chaufray et al. 2015) based on a monthly average Chaufray et al. (2021a). The model was able to reproduce the observations during most of the year but the large brightness measured near the perihelion season (typically  $L_s \sim 210\text{--}300^\circ$ ) was not reproduced suggesting a missing source of atomic hydrogen in the model.

## 2.2.2 O 130.4 nm

Observations of the OI 130.4 nm triplet by SPICAM-UV were used by Chaufray et al. (2009) to derive, for the first time since the Mariner missions in the 1970s, the oxygen density at the

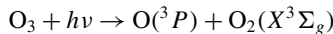
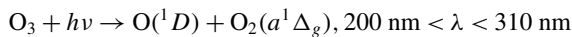
exobase and in the thermosphere of the planet. They fitted the observed emission profiles to an exospheric model coupled to a radiative transfer model. The OI triplet is originated by the transition from the  $O(^3S)$  excited state to the  $O(^3P)$  ground state. The excited state is populated by resonant scattering of solar radiation and by photoelectron impact. Chaufray et al. (2009) found an average O density at the exobase of  $1.2 \times 10^7 \text{ cm}^{-3}$  (with a total uncertainty of about a factor 2–3) for low SZA, with a strong decrease of about a factor of 2 for high values of SZA. They also retrieved a value for the exospheric temperature of about 300 K, from which they inferred the possible presence of a hot oxygen population. Finally, they derived a value of the  $O/CO_2$  mixing ratio at 135 km of 0.9%, decreasing again with increasing SZA. This measurement is of particular importance to constrain computational models, given the dominant role of oxygen in the thermal balance of the thermosphere (e.g. Medvedev et al. (2015)).

To explain the low abundance of  $O_2$ , despite the cumulated hydrogen escape over geological time, the escape of oxygen by the dissociative recombination of  $O_2^+$  ions with electrons had been suggested by McElroy (1972), and its importance confirmed by numerous numerical studies (e.g. Chaufray et al. (2007)). An extended hot oxygen corona produced by this photochemical reaction was also predicted but SPICAM was not sensitive enough to observe it from the limb observations.

## 2.3 Probing Chemistry and Composition

### 2.3.1 $O_2$ Dayglow

The  $O_2(a^1\Delta_g)$  dayglow at 1.27  $\mu\text{m}$  on Mars is produced during ozone photodissociation by solar UV radiation in the Hartley continuum.



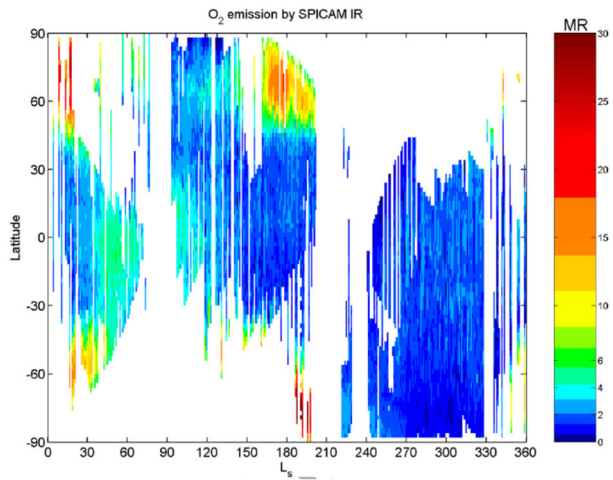
with a quantum yield of 0.9 and 0.1 respectively at wavelengths shorter than 307 nm (Ball et al. 1993; Ball and Hancock 1995).

This emission was discovered on Mars from Earth-based measurements by Noxon et al. (1976). As the  $O_2(a^1\Delta_g)$  dayglow originates from ozone photolysis, it reflects the distribution of ozone that is one of the most chemically reactive species of the Martian atmosphere. The ozone seasonal cycle was first documented by Mariner 9 (Barth et al. 1973) and has since then been considered to anticorrelate with water vapor. Consequently, the  $O_2(a^1\Delta_g)$  dayglow emission should also be sensitive to the  $H_2O$  distribution in the atmosphere of Mars. Thereby, measurements of the  $O_2(a^1\Delta_g)$  dayglow emission and their comparison with photochemical models help to validate the model representation of the water cycle. A summary of the chemistry of ozone on Mars and its observations can be found in Vandaele et al. (2024), this collection, while a detailed description of the water cycle can be found in Montmessin et al. (2024), this collection.

Krasnopolsky (1997) proposed the ground-based monitoring of the emission to study variations of photochemical processes. Relevant observations were performed from 1997 to 2012 and resulted in a rough seasonal-latitude map of  $O_2(a^1\Delta_g)$  based on 13 observing sessions in the period from 1997 to 2012 (Krasnopolsky 2007, 2013).

On Mars Express, three spectrometers cover the wavelength range of the  $O_2$  dayglow and thus may in principle measure it during nadir and limb observations. SPICAM IR has been continuously monitoring the  $O_2(a^1\Delta_g)$  dayglow since 2004. Fedorova et al. (2006) retrieved

**Fig. 6** Latitudinal and seasonal distribution of the  $O_2$  dayglow emission measured by SPICAM IR. Reproduced with permission from Fedorova et al. (2006), copyright by AGU



from SPICAM a first  $O_2(a^1\Delta_g)$  dayglow seasonal-latitudinal map for MY27 (Fig. 6). Altieri et al. (2009) obtained a similar dataset for MY27 and MY28 using OMEGA. The short wavelength channel of PFS also worked in the range of  $1.2\text{--}6\ \mu\text{m}$  with a resolution of  $1.3\ \text{cm}^{-1}$  (Formisano et al. 2005a). Unfortunately, the low signal-to-noise ratio of PFS below  $2\ \mu\text{m}$  prevented measuring the latitude distribution of the  $O_2$  emission for an individual orbit.

The SPICAM and OMEGA datasets produced consistent results (see Fig. 6): the largest dayglow emission is detected in polar regions during equinoxes with maximum values of 30 MR. The highest dayglow intensity of 30 MR was measured in the Southern hemisphere ( $70\text{--}80^\circ\text{S}$  latitudes) at  $L_s = 185\text{--}195^\circ$  and of 26 MR in the northern polar regions (latitudes  $70\text{--}80^\circ\text{N}$ ) at  $L_s = 10\text{--}20^\circ$ . The faintest emission has been reported during the Southern hemisphere summer, near perihelion ( $L_s = 270\text{--}330^\circ$ ), with an upper limit of 1–2 MR. At low latitudes ( $30^\circ\text{S}\text{--}30^\circ\text{N}$ ) the seasonal evolution of the  $O_2(a^1\Delta_g)$  emission showed a distinct maximum (5–7 MR) near aphelion. This is consistent with the maximum of  $O_3$  occurring in the same season, which has been reported by Mars Express from spectral radiance studies (Perrier et al. 2006 and others), and by modeling studies (Lefèvre et al. 2004, 2008).

The analysis of a continuous set of  $O_2(a^1\Delta_g)$  dayglow intensities from SPICAM IR nadir measurements for six Martian years from the end of MY26 to MY32 (Guslyakova et al. 2016) confirmed the first results obtained by SPICAM and OMEGA. Comparison of the data with GCM simulations and simultaneous ozone measurements by SPICAM UV allowed to derive the quenching rate ( $k$ ) of the excited  $O_2$  molecules by  $CO_2$ ,  $k = 0.73 \times 10^{-20}\ \text{cm}^3\ \text{molecules}^{-1}\ \text{s}^{-1}$ .

The long-term dataset analyzed by Guslyakova et al. (2016) allowed studying the inter-annual variations of the  $O_2$  dayglow. It was found that the  $O_2(a^1\Delta_g)$  seasonal pattern is rather stable with average year-to-year relative variation of about 21%, in accord with inter-annual variations detected from the ground (Krasnopolsky 2013). The most variable region corresponds to northern and southern spring at middle latitudes, coinciding with sublimation of the polar caps in both hemispheres. Southern latitudes also show a high year-to-year variability in summer ( $L_s = 270\text{--}330^\circ$ ) relating to the dust activity in this region.

The high spatial resolution of OMEGA allowed to observe gravity waves through  $O_2$  dayglow measurements at  $1.27\ \mu\text{m}$  (Altieri et al. 2009). Waves are found preferentially at high incidence angles and latitudes between  $55^\circ$  and  $75^\circ\text{S}$ . Mesoscale meteorological modeling predicts gravity wave activity in the same range of latitude as the observed  $O_2(a^1\Delta_g)$  wave

patterns with temperature oscillations consistent with existing measurements. This study demonstrated that the airglow imagery can be used to detect the bi-dimensional propagation of gravity waves.

Nadir measurements of the O<sub>2</sub> dayglow were attempted using the ACS NIR spectrometer on TGO, an instrument with a very high resolving power of more than 25,000. Unfortunately, due to extremely low SNR the nadir measurements by NIR were uninformative.

### 2.3.2 N<sub>2</sub> Vegard-Kaplan

SPICAM-UV observations allowed for the first time the identification on Mars of the N<sub>2</sub> Vegard-Kaplan (VK) bands (Leblanc et al. 2006a), predicted almost 30 years before (Fox and Dalgarno 1979). A detailed analysis of the observations by Leblanc et al. (2007) showed that the measured intensities in the VK (0–5) and (0–6) systems presented little SZA and solar activity variations. Based on previous modeling work (Fox and Dalgarno 1979), Leblanc et al. (2007) were able to convert the measured intensity in N<sub>2</sub>/CO<sub>2</sub> column ratio, finding a value of 0.9%. They also deduced that N<sub>2</sub> is in diffusive equilibrium in the thermosphere above about 150 km. The analysis of the scale height of the VK bands also allowed Leblanc et al. (2007) to derive thermospheric temperatures, which were in good agreement with those derived from CO<sub>2</sub> emissions in the same dataset (see Sect. 2.1). The identification of the VK bands motivated the creation or update of different computational models to simulate them and infer the N<sub>2</sub> abundances needed to reproduce the observations. While one of the models (Jain and Bhardwaj 2011) found that a reduction of a factor of 3 of the Viking N<sub>2</sub> mixing ratio is needed to reproduce the observed emission rate, Fox and Hać (2013) were able to reproduce the SPICAM-UV observed intensities without any modification of the N<sub>2</sub> mixing ratio.

## 3 Nightside Emissions: Probing Atmospheric Transport

### 3.1 NO Nightglow

As mentioned in Sect. 1, before Mars Express all attempts to detect emission in the nightside of Mars, motivated partially by previous observations of Venus nightglow, were unsuccessful. Thanks to its sensitivity and to the implementation of a special grazing limb observation mode, just a few months after starting its science phase, the SPICAM UV spectrometer performed the first detection of nightglow on Mars (Bertaux et al. 2005a), featuring H Lyman- $\alpha$  emission (121.6 nm) and the  $\gamma$  and  $\delta$  bands of NO from 190 to 270 nm (see Fig. 1). This later emission is produced by the recombination of N and O atoms.

As in the case of Venus nightglow, it was proposed that N and O atoms were produced by photodissociation on the dayside of the planet and transported towards the nightside by the general circulation, where atoms recombine. Thus, this process can be seen as a tracer of transport in Mars upper atmosphere, and this first observation already suggested a circulation completely different from that of Venus. While the Venus thermospheric circulation was found to be dominated by the subsolar-antisolar (SS-AS) circulation, with maximum emission in the low latitudes and close to midnight (with some departures due to the effects of the Venus superrotation), on Mars, the brightest emission was found over the polar nights, suggesting a strong vertical flow over the polar atmosphere (Bertaux et al. 2005a).

Following this first detection of nightglow, Cox et al. (2008) analyzed 21 orbits of SPICAM nightglow observations. While the NO emission was highly variable, it was found that

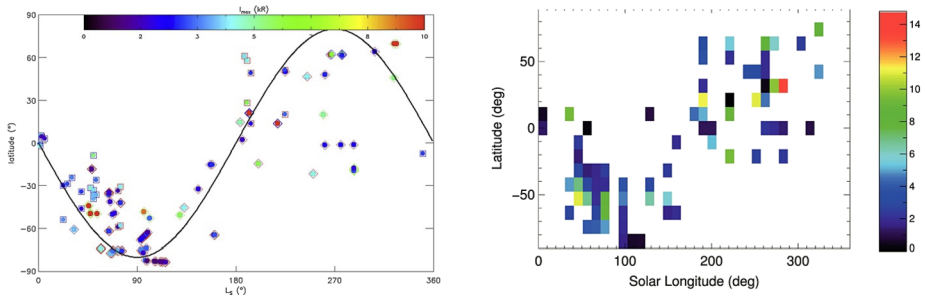


**Fig. 7** Left panel: seasonal and latitudinal distribution of positive NO detections in stellar occultations, from Gagné et al. (2013). Right panel: seasonal and latitudinal variation of the peak NO emission rate, from Stiepen et al. (2015b). Reproduced with permission, copyright by AGU

the emission peak was generally located at lower altitudes in observations obtained at high latitudes in the winter hemisphere, and that most intense emissions usually corresponded with low peak altitudes, hinting to a strong transport towards the polar winter region produced by an intense Hadley cell.

In addition to the usual limb observations, it was found that the NO nightglow produced a detectable contamination in stellar occultation observations performed by the SPICAM-UV channel. Following a similar study in Venus atmosphere, Gagné et al. (2013) developed a method to isolate the “contaminating” NO emission in these occultation observations, increasing significantly the number of observations of the NO nightglow. The analysis of the seasonal and latitudinal variability of the emissions resulted in most emissions concentrating around a sinusoidal curve given by  $\text{Lat} = -80 \times \sin L_s$  (Fig. 7, left).

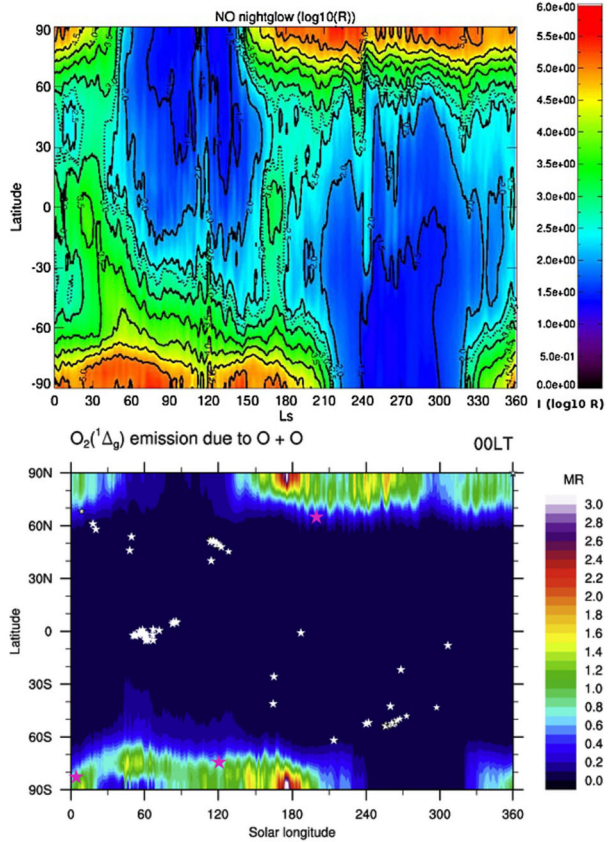
The observations were compared with predictions by the LMD-Mars Global Climate Model (LMD-MGCM) (Forget et al. 1999; González-Galindo et al. 2009). The LMD-MGCM predicted the most intense emissions in the polar winters during solstices and at both polar regions during equinoxes, as shown in Fig. 8. While the predicted behavior during solstices was overall confirmed by the observations, interesting discrepancies were also found, such as the absence of intense observed emission in the polar regions around equinoxes, suggesting deficiencies in the predicted general circulation.

Stiepen et al. (2015b) combined all the NO nightglow data obtained during the life of SPICAM UV using both limb and stellar occultation observations, forming a dataset of around 200 positive NO nightglow detections from a total of about 5000 analyzed observations. The distribution of the observations follow the same sinusoidal pattern identified by Gagné et al. (2013) (Fig. 7, right), confirming to first order the LMD-MGCM prediction of strongest emission in the polar winters consistent with a strong descent of air in the polar night.

### 3.2 O<sub>2</sub> Nightglow

The O<sub>2</sub>( $a^1\Delta_g$ ) nightglow at 1.27  $\mu\text{m}$  is a product of atomic oxygen recombination that, in turn, as in the case of the NO nightglow, is a product of photolysis of atmospheric gases on the dayside. This nightglow was well known on Venus and allowed to study the circulation of the atmosphere at altitudes of 90–110 km (in the upper mesosphere and the lower thermosphere) (Bougher and Borucki 1994; Gérard et al. 2008b; Gorinov et al. 2018) where the SS-AS circulation is prevailing with some variable contribution of the superrotation zone.

**Fig. 8** Top panel: latitudinal and seasonal distribution of the NO emission rate, in logarithmic scale, simulated by the LMD-MGCM, from Gagné et al. (2013). Bottom panel: same for the  $O_2(a^1\Delta_g)$  vertical emission (linear scale) produced by the  $O + O$  recombination (MR). Locations where OMEGA detected an emission (three pink stars) are in the regions where the model predicts a substantial intensity, while observations without detection (white stars) are outside these regions. From Bertaux et al. (2012). Note that, despite the differences in the color scales, the predicted pattern of emission is quite similar for both systems. Reproduced with permission, copyright by AGU

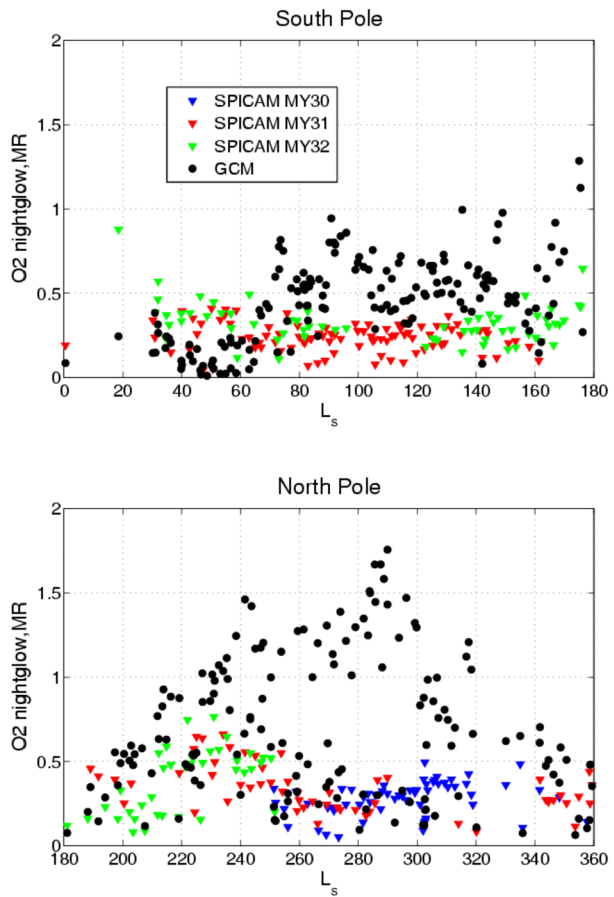


The SS-AS circulation brings the oxygen atoms, formed as a result of  $CO_2$  photodissociation in the dayside, to the nightside. At the antisolar point, the air descends, and the excited oxygen molecules are formed and emitted the photons at wavelength of  $1.27 \mu m$ .

On Mars, the  $O_2$  nightglow at  $1.27 \mu m$  has the same nature as on Venus, but since its predicted intensity was below 50kR (Krasnopolsky 2003; García Muñoz et al. 2005) it was not unambiguously detected until Mars Express. A tentative detection was reported by Krasnopolsky (2003), but a large field of view of their observations hampered the detection of the nightside emission by oxygen recombination due to a possible contamination of a residual dayglow.

The first firm observations of the  $O_2$  nightside emission were provided by OMEGA observing the limb, obtaining 3 vertical profiles out of 40 observations (Bertaux et al. 2012). The emission was detected in the southern and northern polar regions, during the polar night, with intensity  $\sim 0.240$  MR. To explain the observed emission rate, the LMD-MGCM model was adapted and validated. The LMD-MGCM simulates the large Hadley cell characterizing the meridional circulation, ascending from the summer pole and descending to the winter pole. Detectable emission is predicted only at latitudes higher than  $60^\circ$ , over a rather extended season centered on the polar winter, and absent during the polar summer (Fig. 8). As for the NO nightglow, at both equinoxes the model predicts simultaneous emission in both polar regions. It was shown that the  $O_2$  emission on Mars, as well as the NO nightglow, allows tracing a downward advection transport mechanism, though at a lower altitude

**Fig. 9** Seasonal variations of the O<sub>2</sub> nightglow for the North (bottom) and the South (top) poles for 3 Martian years (30–32) in latitude bin: 65°–90°. Colors designate different years of SPICAM observations. The black circles are the corresponding GCM results



range than in the case of the NO nightglow. However, the predicted pattern of emission is remarkably similar for both systems.

These detections were confirmed almost simultaneously by limb observations by the CRISM instrument on the Mars Reconnaissance Orbiter mission (Clancy et al. 2012).

Motivated by these OMEGA observations, Fedorova et al. (2012) used the SPICAM IR channel to search the O<sub>2</sub> nightglow. The emission rate observed by OMEGA was too weak to allow observation in SPICAM IR nadir observations, so the search of the nightglow was performed only in limb measurements. In 2010 vertical profiles of the emission were obtained near the South Pole at latitudes of 82–83°S for two sequences of observations:  $L_s = 111\text{--}120^\circ$  and  $L_s = 152\text{--}165^\circ$ . Averaged vertically integrated intensity of the emission showed an increase from 0.22 to 0.35 MR consistent with the OMEGA observations. The altitude of the emission maximum varied from 45 km on  $L_s = 111\text{--}120^\circ$  to 38–49 km on  $L_s = 152\text{--}165^\circ$ . Comparison with the LMD-MGCM shows that modeled O<sub>2</sub>( $a^1\Delta_g$ ) nightglow reproduced fairly well the SPICAM observations, even though the vertically-integrated emission appeared to be overestimated in the model (Fig. 9). Moreover, based on the O<sub>2</sub> emission vertical profiles, the CO<sub>2</sub> density and the temperature from the SPICAM UV observations, the density of oxygen atoms was derived at altitudes from 50 to 65 km, varying from  $1.5 \times 10^{11}$  to  $2.5 \times 10^{11}$  cm<sup>-3</sup>. The atomic oxygen is known to have an important effect



on the 15  $\mu\text{m}$  cooling of the  $\text{CO}_2$  atmosphere, as collisions with oxygen excite the vibrational states of  $\text{CO}_2$ , enhancing the emission rate and the cooling (Forget et al. 2009). As a consequence, an accurate knowledge of atomic oxygen density in the middle atmosphere is of high importance for a correct simulation of mesospheric and thermospheric temperatures.

Very recently, the visible counterpart of the  $\text{O}_2(a^1\Delta_g)$  emission, the  $\text{O}_2$  Herzberg bands, has been observed for the first time on Mars nightside by the UVIS channel of NOMAD (Gérard et al. 2023). This emission is also formed during the recombination of O atoms produced in the dayside and transported to the nightside, so it also traces atmospheric transport. Positive detections concentrate on the polar winter regions, generally poleward of latitude 60, with altitude between 34 and 60 km and typical limb brightness of a few hundreds kR, so they should be visible to the naked human eye. The possibility of simultaneous observations of the  $\text{O}_2$  Herzberg bands and the NO nightglow by UVIS opens the door to studying the different transport regimes at different altitudes, posing stronger constraints to global climate models.

## 4 Aurora

### 4.1 Discrete Aurora

Auroral emissions were first detected on the Martian nightside with SPICAM by Bertaux et al. (2005b) during a limb observation over a region of strong crustal magnetic field. A sudden increase in the brightness of the Cameron bands was observed during 7 s as shown in Fig. 10. During this period, the spectra showed the presence of the Cameron bands of CO and the  $\text{CO}_2^+$  UVD. On the nightside, these emissions are the unambiguous signature of the collisions of energetic electrons, with  $\text{CO}_2$  molecules populating the  $\text{CO}_2(a^3\Pi)$  and the  $\text{CO}_2^+(B^2\Pi_u)$  excited states. These ultraviolet emissions had been extensively observed in the Mars dayglow during the Mariner flybys and later by Mars Express (see Sect. 2.1.1). The CO Fourth Positive system corresponding to the  $A^1\Pi \rightarrow X^1\Sigma$  transition was also observed between 125 and 170 nm. Maximum measured brightness was about 700 R for the Cameron bands and 71 R for the UV doublet, later revised to 2 kR and 200 R respectively by Leblanc et al. (2006b).

The observed emission was strongly localized, with latitudinal extent of the aurora at the limb of about  $30 \pm 2$  km, suggesting that its origin is the precipitation of electrons along crustal magnetic field lines. Although no vertical limb scan of the aurora was obtained, an indirect method was used to determine the altitude of the emission. Bertaux et al. (2005b) used the delay of the light curves of the auroral detection in the different SPICAM spatial bins to estimate the actual altitude of the emission. Knowing the altitude of the MEx spacecraft and its horizontal velocity, the spacecraft-aurora distance may be evaluated and the apparent altitude converted to real altitude. Using this method, the altitude of the observed emission peak was estimated as  $129 \pm 13$  km.

The characteristics of this detection were re-analyzed by Leblanc et al. (2006b) who revised the SPICAM calibration and discussed the geometry of the observation. Based on the intensity ratio of the Cameron bands relative to the UV doublet, they suggested that the UV aurora was produced by electrons with an energy distribution peaking at a few tens of eV. They estimated that an intense flux of low-energy electrons, perhaps an order of magnitude stronger than the typical magnetosheath distribution observed by the Mars Global Surveyor (MGS) mission (Mitchell et al. 2001) or by ASPERA-3 would be precipitated during the observed event. They pointed out that auroral-type peaked electron distributions such as

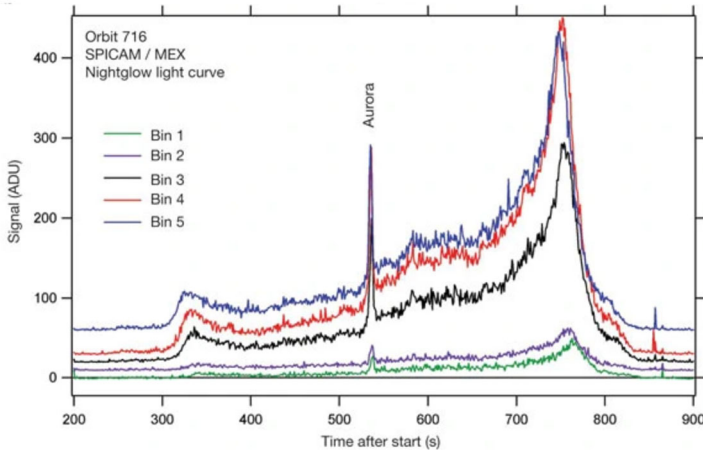


**Fig. 10** Time evolution of the count rate corresponding to the Cameron bands. The abrupt increase at  $t = 530$  s was observed in all five spatial bins of the SPICAM instrument. It corresponds to the first detection of an auroral event. Reproduced with permission from Bertaux et al. (2005b), copyright by Nature Publishing Group

measured by MGS (Brain et al. 2006) and Mars Express (Lundin et al. 2006a,b) would have produced a different distribution of the emissions than observed.

Concurrent measurements between SPICAM, ASPERA-3 and Mars Advanced Radar for Subsurface and Ionosphere Sounding (MARSIS) described by Leblanc et al. (2008) confirmed the spatial correlation between electron precipitation and auroral UV emissions. They observed 8 nadir detections of auroral events on the nightside, all located near regions of crustal magnetic fields in the southern hemisphere. The occurrence of these events was well correlated with the probability to be located in a region of open magnetic field showing cusp-like structures. They also noted that these events were temporally associated with precipitating energetic electrons measured with ASPERA-3 and with an increase in the electron content measured by MARSIS. They pointed out that the increase in the electron density measured at the spacecraft altitude was not necessarily proportional to the brightness of the CO Cameron bands in the associated aurora.

In addition, MARSIS measured the phase distortion produced by the ionosphere. The total electron content (TEC) below the spacecraft was analyzed for 750 MEx orbits and showed positive correlations with the crustal field, which was interpreted as the possible signature of enhanced ionization produced by precipitation of particles along field lines (Safaenili et al. 2007). However, no relation was found between the TEC values and the electron energy flux measured during the events (Leblanc et al. 2008). A possible explanation is that the electrons measured by ASPERA-3 did not precipitate below the MEx spacecraft where the TEC was measured.

Figure 11 illustrates the time evolution of the downward electron energy flux measured by ASPERA-3, the energy spectrum measured by MGS/ER and the SPICAM signal along a MEx orbit. The total energy flux increased by one order of magnitude at the time of the auroral detection.

An analysis of the full SPICAM nightside database (nadir and limb) was made by Gérard et al. (2015) and Soret et al. (2016). Gérard et al. (2015) re-analyzed all SPICAM nadir observations collected between January 2004 and March 2014, together with Analyzer of Space Plasma and Energetic Atoms (ASPERA-3) measurements of energetic downgoing

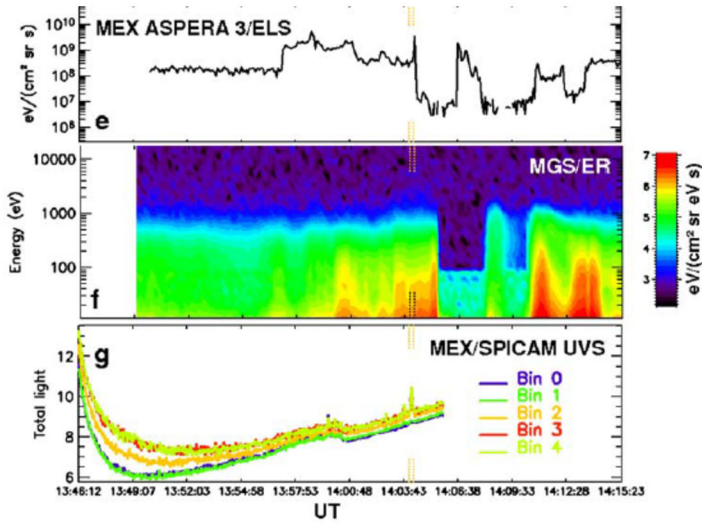


**Fig. 11** Time evolution along a segment of MEX orbit of (e) the downward ASPERA-3/ELS electron energy flux, (f) electron flux measured by the MGS MAG/ER instrument, and (g) the SPICAM total UV intensity in the different spatial bins. The yellow vertical dotted lines indicate the detections of auroral events. Reproduced with permission from Leblanc et al. (2008), copyright by AGU

electrons. They identified 16 detections of FUV auroral events collected over 9 MEX orbits. They confirmed that the aurorae were located near the statistical boundary between open and closed field lines in cusp structures, as measured at 400 km with the magnetometer on board the MGS. All detections were located in the southern hemisphere between  $17.3^{\circ}\text{S}$  and  $64.1^{\circ}\text{S}$  and between  $158^{\circ}$  and  $214^{\circ}$  longitude, a region of relatively strong crustal magnetic field as seen in Fig. 12. The observed nadir brightness of the CO Cameron bands occasionally reached 2.0 kR. A majority of the passes over the crustal regions at different times and dates did not identify the presence of UV auroral events. This suggested that the Martian aurora was either infrequent or that most of them reached brightness below the SPICAM detection threshold. The aurora was not detected on successive MEX orbits. This characteristic suggested that the aurorae may be short-lived or significantly changing brightness over a time period shorter than the orbit period (6.75 hours). The latitudinal width of the aurora was observed to vary from less than 20 km to 120 km, with a mean value of 44 km.

Three auroral detections at the limb were analyzed by Soret et al. (2016) using the method described by Bertaux et al. (2005b). The altitude values were 132, 143 and 137 km. An example of corrected limb profile of the Cameron and UVD emissions is shown in Fig. 12.

Concurrent measurements of the electron precipitation were made with the ASPERA-3 ELS instrument to investigate the relation between the electron flux measured at the spacecraft altitude and the ultraviolet auroral signature. ELS provided measurements of the electron energy spectra between 10 eV and 20 keV. The measured downward energy flux in the vertical direction contemporaneous to the auroral detections ranged from 0.1 to  $13 \text{ mW m}^{-2}$ . The mean energy of the electron energy spectra during these measurements with ASPERA-3 ranged from 150 to 280 eV. The correlation between the auroral brightness and the down-going energy flux measured at higher altitude with ASPERA-3 ELS was low. This lack of proportionality between the two quantities was also noticed by Leblanc et al. (2008). It may be a consequence of the distance between the in situ electron measurements and the aurora and possible acceleration below the spacecraft. The location of the auroral magnetic

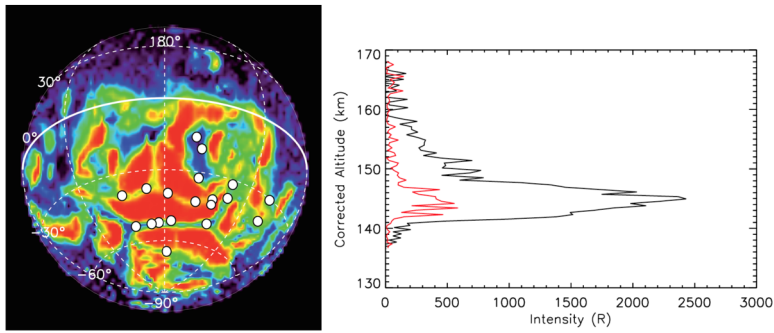


**Fig. 12** Left: locations of the auroral events detected with SPICAM. The background color indicates the statistical probability to find a closed magnetic field line at the altitude of 400 km (Brain et al. 2007) from 100% closed (red) to 100% open (dark blue) (credit: Gérard-Soret, ESA); right: altitude distribution of the Cameron (black) and  $\text{CO}_2^+$  UV doublet (red) emissions at the limb. The altitudes have been corrected for the distance between the aurora and the tangent point of the line of sight. Reproduced with permission from Soret et al. (2016), copyright Elsevier Inc

footprint of the maximum electron flux could be several degrees of latitude away from the sub-satellite latitude. This finding suggests that the field lines threading the auroral electron events may be significantly tilted from the vertical at the altitude of the MEx spacecraft (Gérard et al. 2015).

Monte Carlo simulations (Shematovich et al. 2008; Gérard et al. 2008a) were used to convert altitude profiles of FUV emissions to equivalent monoenergetic electron energy. Soret et al. (2016) calculated volume emission rates and nadir brightness of the Cameron,  $\text{CO}_2^+$  UVD, CO Fourth Positive, OI 130.4 and 135.6 nm emissions for initial electron energy flux of  $1 \text{ mW m}^{-2}$  and mean electron energies between 50 and 1000 eV. They also calculated the emissions associated with two electron energy spectra measured by ASPERA-ELS concurrently to auroral events. They found that the brightness of the UVD increased from 490 R at 50 eV to 1700 R at 1 keV. Similarly, the intensity of the Cameron bands increased from 1.25 kR to 4.3 kR. It should be noted that recent re-measurements of the emission cross sections of the Cameron bands by impact on  $\text{CO}_2$  have significantly modified the cross section value (Lee et al. 2022).

## 4.2 Proton Aurora

Proton aurora on the dayside of Mars was first observed by the Imaging UltraViolet Spectrograph (IUVS) instrument on board MAVEN in the form of anomalous thermospheric H Ly-alpha emission (Deighan et al. 2018) (see Sect. 5) and attributed to precipitating solar wind protons undergoing charge-exchange with atmospheric H atoms.

Motivated by this discovery, Ritter et al. (2018) analyzed the SPICAM dataset to identify and analyze Lyman- $\alpha$  enhancements as possible signatures of precipitation of fast protons/H atoms. They examined the SPICAM spectra collected between July 2004 and May 2011, a period of declining solar activity, and identified 18 proton auroral events. The signature of these events was an excess Lyman- $\alpha$  brightness usually in the 100 to 150 km region. By contrast with the dayglow emission, the Lyman- $\alpha$  auroral emission is optically thin and Doppler shifted out of the thermal H distribution (Gérard et al. 2019). Thus, proton aurorae are identifiable in FUV spectral data as an emission enhancement of intensities between 110 and 150 km in the Lyman- $\alpha$  altitude-intensity profile. To identify proton aurorae, they

used the Lyman- $\alpha$  intensity ratio between two altitude ranges  $I(120\text{--}150\text{ km})/I(160\text{--}190\text{ km})$  combined with visual inspection which proved to be reasonable for their survey. After identifying potential candidates, they examined solar and interplanetary in situ data from the Solar and Heliospheric Observatory (SOHO), Advanced Composition Explorer (ACE) and Geostationary Operational Environmental Satellites (GOES) missions.

Figure 13 shows an example of a strong event observed on 26 February 2005, following an Interplanetary Co-rotating Interaction Region (CIR) and a possible Interplanetary Coronal Mass Ejection (ICME). The intensity enhancements ranged between 0.7 and 3 kR with peaks located between 120 and 150 km. Strong, clearly identified Lyman- $\alpha$  enhancements on the dayside were observed in 4% of the orbits. Taking weaker events into account, a fraction of 13% of the orbits with appropriate observing conditions were associated with a detection. The comparison of all SPICAM data with the HELCATS ARRCAT catalogue revealed that no ICME was predicted to reach Mars when SPICAM did not detect a proton aurora. No conclusion could be reached concerning the presence or not of CIRs during this period. Among these, the six strong cases were associated with a ICME and/or a CIR reaching Mars at the time of the observations.

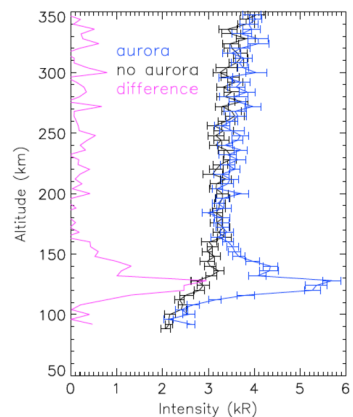
## 5 Mars Express as Precursor to Later Missions

The many discoveries about airglow and aurora provided by Mars Express boosted the interest in these fields, and later missions were equipped with instruments dedicated among others to observing these atmospheric emissions. We describe here briefly the main discoveries about airglow and aurora provided by MAVEN and EMM.

### 5.1 MAVEN

MAVEN, a NASA mission devoted to the study of the upper atmosphere, its interaction with the sun and the implications for the long-term evolution of Mars (Jakosky et al. 2015), was launched in 2014. Its payload includes IUVS, able to measure UV spectra (120–330 nm) with four observing modes: (1) limb scans near periapsis; (2) planetary mapping at two spectral resolutions; (3) coronal mapping; (4) stellar occultations (McClintock et al. 2015). IUVS has significantly expanded our knowledge of the Mars airglow and aurora.

**Fig. 13** Example of Lyman- $\alpha$  limb profile of a proton aurora. The blue curve shows the total intensity, the black curve is the dayglow resonance scattering contribution and the purple curve is the difference, equal to the proton aurora contribution. Reproduced with permission from Ritter et al. (2018), copyright by AGU



### 5.1.1 Dayglow Emissions

Observations of the CO<sub>2</sub> dayglow during more than 6 years have shown a strong correlation between the thermospheric temperature, the season and the solar forcing, and also strong local time variations and effects of non-migrating tides (Jain et al. 2023). The correlation with solar activity is in contradiction with SPICAM results, which may be related to the smaller SPICAM dataset or to the joint use of Cameron bands and CO<sub>2</sub><sup>+</sup> UVD in Stiepen et al. (2015b), as discussed in Sect. 2.1. Also the effects on the thermospheric temperatures of solar flares and of the 2018 global dust storm have been studied with IUVS. Jain et al. (2018) found that a strong X-class flare on 10 September 2017 increased the thermospheric temperatures in up to ~70 K, but after 4.5 hours the temperatures were back to their normal values, suggesting a fast recovery after the flare. Jain et al. (2020) found that the thermospheric temperatures increased in ~20 K due to the MY34 global dust storm, and also the latitudinal variations of temperature were affected by the modifications of the atmospheric dynamics by the storm.

IUVS observations have also improved our knowledge on the exosphere and the escape rates contributing together with SPICAM observations to a shift of paradigm thoroughly discussed in Montmessin et al. (2024), this collection. Using echelle observations sensitive to H and D in the thermosphere, Clarke et al. (2017) confirmed the presence of strong seasonal variations in the H and D escape rates. Using regular coronal observations sensitive to H in the corona, Chaffin et al. (2018) found that the incorporation of a hot H component to the analysis of IUVS observations reproduces better the observed emission profile and also found strong seasonal variations. Chaufray et al. (2021b) combined low resolution Lyman-alpha observations with echelle observations when available to derive D/H values at 80 and 200 km at 4 different periods. Later analysis of the echelle dataset showed that D brightness presents, in addition to its seasonal variation, significant variations with timescale of hours to days, due to solar energetic particles, solar flares and the 28-day solar rotation (Mayyasi et al. 2017).

The accumulation of data during the MAVEN mission has also allowed to study the interannual variation in the H escape rate, finding a week response to the MY34 global dust storm, which was attributed to enhanced temperatures suppressing the diffusion of H atoms to high altitudes (Mayyasi et al. 2023). Solar cycle effects on the escape were also identified, though masked by the larger seasonal variability (Mayyasi et al. 2023).

Regarding O escape, systematic observations by IUVS allowed identification of the hot oxygen corona predicted but not observed by SPICAM (see Sect. 2.2.2) based on the change of scale height in the vertical profile of the O 130.4 brightness (Deighan et al. 2015).

New information about the composition of Mars upper atmosphere has also been achieved with IUVS observations. Identification of the N<sub>2</sub> Lyman-Birge-Hopfield (LBH) and VK bands allowed deriving N<sub>2</sub> abundances in the thermosphere, finding that the retrieved values were larger than GCM predictions at 130 km, but agree well with the model at 150 km (Stevens et al. 2015). Analysis of NO  $\gamma$  bands observations on the dayside allowed retrieving NO thermospheric densities Stevens et al. (2019), which agreed reasonably with model predictions, but were significantly lower than the values obtained by in-situ measurements during Viking descent. Lo et al. (2022) analyzed CI 156.1 nm and 165.7 nm dayglow to derive C abundances for the first time. The retrieved C abundance was higher than predicted by a photochemical model, and a variation in the emission peak altitude with season was also obtained.

### 5.1.2 Nightglow Emissions

IUVS has also significantly contributed to the study of the NO nightglow, greatly improving the seasonal and latitudinal coverage achieved by SPICAM. The analysis of vertical profiles of NO emission obtained during limb observations (Stiepen et al. 2017) revealed strong seasonal and geographical variations linked to the supply of N atoms to the nightside. Comparisons with the LMD-MGCM showed a systematic overestimation of the emission peak altitude by the model of about 20 km. Hints of longitudinal variations produced by planetary waves were also found (Stiepen et al. 2017). A later study using apoapse imaging confirmed the presence of strong longitudinal variations due to tides, both at the equator during equinox and at the polar regions during winter seasons (Schneider et al. 2020), usually well reproduced by the LMD-MGCM. It was also found, though, that the model underestimates the emission rate by a factor of almost 2, due probably to the underestimation of the dayside production of N and O (Schneider et al. 2020).

### 5.1.3 Aurora

Following the unexpected discovery of aurorae by Mars Express, Schneider et al. (2021) and Soret et al. (2021) analyzed the IUVS dataset to identify a total of 278 discrete auroral events. They confirmed that aurorae occur occasionally, mainly in the vicinity of a crustal magnetic field and in the so-called “sailboat” region, between  $150^\circ$  and  $210^\circ$  longitude and  $30^\circ$  to  $60^\circ$  south latitude. However, they unexpectedly detected discrete aurorae outside of the crustal magnetic field structure, in the northern hemisphere. They also showed that discrete aurorae are brighter in the strong magnetic field area, though the presence of a crustal magnetic field does not influence the altitude of the auroral emission peak at  $124.4 \pm 17$  km, and tend to statistically occur more often in the evening than in the morning. Finally, based on the brightness of the oxygen line at 297.2 nm, they estimated the nightside oxygen green line intensities to reach up to a few kiloRayleighs, a brightness visible with the naked eye.

Several studies using IUVS data aimed at deriving correlations between auroral signatures and the Mars environment. Girazian et al. (2022) showed that high solar wind pressures increase the IUVS auroral detection frequency but not the brightness of the emission. Xu et al. (2022) established a causal correlation between in situ measurements of accelerated electron events and the characteristics (locations, crustal field, etc.) of the auroral events. The global plasma modeling by Fang et al. (2022) predicted that aurorae tend to occur more frequently in small-scale patches near strong crustal fields and when coronal mass ejections (CMEs) impact Mars, in agreement with Schneider et al. (2021), Soret et al. (2021) and Girazian et al. (2022).

Following its discovery Deighan et al. (2018), further studies of the occurrence, seasonal dependence and control by solar activity of the proton aurora have been published based on IUVS observations (Hughes et al. 2019; Chaffin et al. 2022b). Dayside proton aurorae were found to be quite common with a global occurrence of 14% of the IUVS periapsis data. They occur preferentially near northern winter solstice, reaching a frequency of nearly 100%, making it the most common type of Martian aurora. The seasonal variation is a consequence of the increased size of the H corona near  $L_s = 270^\circ$  combined with the larger interaction with the solar wind, higher atmospheric temperatures and solar wind flux near perihelion. All these factors contribute to increasing the frequency and intensity of the proton aurora.

A third type of auroral event was discovered in 2015 with IUVS: the diffuse aurora, originated by the global precipitation of solar energetic particles. Contrary to the discrete aurora,

diffuse aurora cover a large fraction of the nightside of the planet. Two events have been detected so far, in December 2014 (Schneider et al. 2015) and September 2017 (Schneider et al. 2018). During these diffuse auroral events, that can last several days, a global brightening of the planet occurs as low as  $\sim 60$  km. The CO Cameron bands, the  $\text{CO}_2^+$  UVD and the [OI] emission at 297.2 nm are observed, similarly to discrete aurorae. A strong correlation was found with MAVEN's Solar Energetic Particle (SEP) and Solar Wind Electron Analyzer (SWEA) measurements, suggesting that diffuse aurorae result from the interaction of solar energetic particles (SEPs) with the Martian atmosphere. These particles, which are 100 to 1000 times more energetic than those causing discrete aurorae, can reach much lower altitudes in the atmosphere.

## 5.2 EMM

EMM was launched in 2020 with the main scientific goals of studying the connections between the lower, the upper atmosphere, and the atmospheric escape (Almatroushi et al. 2021). The Emirates Mars Ultraviolet Spectrometer (EMUS) is an imaging spectrograph covering the spectral range 100–170 nm (Holsclaw et al. 2021), measuring for the first time the EUV part of the spectrum.

Since 2021, EMUS has been monitoring the Mars nightside in the far ultraviolet. Its distant orbit allows to almost observe the entire disk of the planet at once. New emissions have been identified providing information on the coupling of the upper atmosphere with the solar input and on the escape (Jain et al. 2022; Chaffin et al. 2022a). Lillis et al. (2022) described oxygen auroral signatures at 130.4 nm. They detected aurorae in 77% of the EMUS images and confirmed that the highest occurrence rates and brightness are found in regions of open magnetic field lines, in agreement with the Mars Express detections.

The unexpected presence of patchy proton aurora has been observed on the dayside with EMUS (Chaffin et al. 2022b). These emissions were observed in about 2% of the EMUS disk images. Patchy aurorae are quite dim and broadly dispersed features that occur away from strong crustal fields. Sinuous aurorae present a thin elongated serpentine structure stretching thousands of kilometers into the nightside from near midnight in the northern hemisphere. No clear explanation has been proposed so far for such behaviors. Finally, Lillis et al. (2022) mention that many more varied shapes and patterns than those three types of aurorae (discrete, patchy and sinuous) in the EMUS aurora data set can be observed, proving that the Mars' magnetotail environment is highly dynamic.

## 6 Summary and Perspectives

The start of the science mission of Mars Express back in 2003 marked the beginning of a golden era in the study of the airglow and aurora on Mars. For the first time since the Mariner missions in the 70s, systematic observations of the UV and IR atmospheric emissions allowed for an unprecedented characterization of the processes originating them. As a result, an impressive amount of highly valuable information about the temperatures, density, composition and dynamics of the upper atmosphere has been obtained, which have, for example, revolutionized our understanding of the atmospheric escape, with important implications for the long-term evolution of the Martian system. Mars Express observations also opened a full new topic of research by the discovery of the presence of aurorae on Mars. These pioneering Mars Express observations have been later expanded and complemented by observations by the ExoMars TGO, MAVEN and Mars Emirates missions.



After 20 years of Mars Express observations, an impressive amount of data has been collected, and there is still work to do until the analysis of the Mars Express datasets can be considered as complete. As an example, a full exploitation of the CO<sub>2</sub> 4.3 μm emissions by OMEGA and PFS with the aim of deriving temperature and density profiles is still awaiting. While additional Mars Express observations of the UV airglow and the aurora are not possible due to the failure of the SPICAM UV channel in 2014, further observations of the IR atmospheric emissions by OMEGA and PFS are still possible. ASPERA-3 also continues to observe the electron and ion fluxes above aurorae. Similarly, the instruments NOMAD and ACS on board ExoMars TGO continue operating nominally and observing the Martian atmosphere in the IR and UV spectral ranges. Thus, the European characterization of the Martian airglow and aurora, in close cooperation with other international teams in the frame of the MAVEN and Mars Emirates missions, is expected to continue providing fascinating results in the years to come.

In a more distant future, at the moment of writing this lines no mission devoted to study the Martian atmosphere has been adopted by ESA or NASA in the years to come. A proposal for a Mars mission, called M-MATISSE and aimed at the characterization of the couplings between the magnetosphere, the thermosphere, and the ionosphere, is currently in competition for the next ESA M7 mission (Sanchez-Cano et al. 2022). If adopted, M-MATISSE will be able to map auroral emissions in the nightside simultaneously to the drivers of the auroral emission, potentially advancing significantly in our understanding of the processes resulting in the different auroral emissions on Mars.

It is also important to mention that the experience gained by the European teams about the airglow and aurora on Mars can be extremely useful in view of the future ESA mission to Venus, EnVision (Widemann et al. 2022). While the main goal of the mission is not the study of the upper atmosphere of Venus, the EnVision payload includes UV and IR spectrometers that could potentially be used to study atmospheric emissions on Venus.

**Acknowledgements** F. González-Galindo and M.A. López-Valverde were funded by Spanish Ministerio de Ciencia, Innovación y Universidades, the Agencia Estatal de Investigación and EC FEDER funds under project PID2022-137579NB-I00 and acknowledge financial support from the Severo Ochoa grant CEX2021-001131-S funded by MCIN/AEI/ 10.13039/501100011033. J.-C. Gérard and L. Soret acknowledge funding by the Belgian Science Policy Office (BELSPO), with the financial and contractual coordination by the ESA Prodex Office (PEA 4000140863). Jean-Yves Chaufray is funded by the Centre National d'Etudes Spatiales and by Programme National de Planetologie and Programme National Soleil-Terre. The authors thank the International Space Science Institute (ISSI) in Bern, Switzerland for the support in producing this collection of papers.

**Funding** Open Access funding provided thanks to the CRUE-CSIC agreement with Springer Nature.

## Declarations

**Competing Interests** The authors have no financial interests attached to the scientific results presented in this report. F. González-Galindo is a Guest Editor of the collection “Mars Express: Pioneering Two Decades of European Science and Exploration of Mars”, but has not been involved in the peer review process of this article.

**Open Access** This article is licensed under a Creative Commons Attribution 4.0 International License, which permits use, sharing, adaptation, distribution and reproduction in any medium or format, as long as you give appropriate credit to the original author(s) and the source, provide a link to the Creative Commons licence, and indicate if changes were made. The images or other third party material in this article are included in the article's Creative Commons licence, unless indicated otherwise in a credit line to the material. If material is not included in the article's Creative Commons licence and your intended use is not permitted by statutory regulation or exceeds the permitted use, you will need to obtain permission directly from the copyright holder. To view a copy of this licence, visit <http://creativecommons.org/licenses/by/4.0/>.

## References

- Almatroushi H, AlMazmi H, AlMheiri N et al (2021) Emirates Mars Mission characterization of Mars atmosphere dynamics and processes. *Space Sci Rev* 217:89. <https://doi.org/10.1007/s11214-021-00851-6>
- Altieri F, Zasova L, D'Aversa E et al (2009) O<sub>2</sub> 1.27 μm emission maps as derived from OMEGA/MEx data. *Icarus* 204:499–511. <https://doi.org/10.1016/j.icarus.2009.07.022>
- Anderson DE (1974) Mariner 6, 7 and 9 ultraviolet spectrometer experiment: analysis of hydrogen Lyman-Alpha data. *J Geophys Res* 79:1513–1518. <https://doi.org/10.1029/JA079i010p01513>
- Anderson DE, Hord CW (1971) Mariner 6 and 7 ultraviolet spectrometer experiment: analysis of hydrogen Lyman-Alpha data. *J Geophys Res* 76:6666–6673. <https://doi.org/10.1029/JA076i028p06666>
- Aoki S, Gkouvelis L, Gérard JC et al (2022) Density and temperature of the upper mesosphere and lower thermosphere of Mars retrieved from the OI 557.7 nm dayglow measured by TGO/NOMAD. *J Geophys Res, Planets* 127(6):e07206. <https://doi.org/10.1029/2022JE007206>
- Ball SM, Hancock G (1995) The relative quantum yields of O<sup>2</sup>(a<sup>1</sup>Δ<sub>g</sub>) from the photolysis of ozone at 227 K. *Geophys Res Lett* 22:1213–1216. <https://doi.org/10.1029/95GL01007>
- Ball SM, Hancock G, Murphy IJ et al (1993) The relative quantum yields of O<sub>2</sub>(a<sup>1</sup>Δ<sub>g</sub>) from the photolysis of ozone in the wavelength range 270 nm ≤ λ ≤ 329 nm. *Geophys Res Lett* 20:2063–2066. <https://doi.org/10.1029/93GL02494>
- Barabash S, Fedorov A, Lundin R et al (2007) Martian atmospheric erosion rates. *Science* 315:501–503. <https://doi.org/10.1126/science.1134358>
- Barabash S, Holmström M, Ramstad R et al (2024) The Induced Magnetosphere of Mars and the Near-Mars environment as Revealed by Mars Express. *Space Sci Rev* 220
- Barth CA, Hord CW, Pearce JB et al (1971) Mariner 6 and 7 ultraviolet spectrometer experiment: upper atmosphere data. *J Geophys Res* 76(10):2213. <https://doi.org/10.1029/JA076i010p02213>
- Barth CA, Stewart AI, Hord CW et al (1972) Mariner 9 ultraviolet spectrometer experiment: Mars airglow spectroscopy and variations in Lyman alpha. *Icarus* 17(2):457–468. [https://doi.org/10.1016/0019-1035\(72\)90011-5](https://doi.org/10.1016/0019-1035(72)90011-5)
- Barth CA, Hord CW, Stewart AI et al (1973) Mariner 9 ultraviolet spectrometer experiment: seasonal variation of ozone on Mars. *Science* 179:795–796. <https://doi.org/10.1126/science.179.4075.795>
- Bertaux JL, Leblanc F, Perrier S et al (2005a) Nightglow in the upper atmosphere of Mars and implications for atmospheric transport. *Science* 307(5709):566–569. <https://doi.org/10.1126/science.1106957>
- Bertaux JL, Leblanc F, Witasse O et al (2005b) Discovery of an aurora on Mars. *Nature* 435(7043):790–794. <https://doi.org/10.1038/nature03603>
- Bertaux JL, Gondet B, Lefèvre F et al (2012) First detection of O<sub>2</sub> 1.27 μm nightglow emission at Mars with OMEGA/MEX and comparison with general circulation model predictions. *J Geophys Res, Planets* 117:E00J04. <https://doi.org/10.1029/2011JE003890>
- Bougher SW, Borucki WJ (1994) Venus O<sub>2</sub> visible and IR nightglow: implications for lower thermosphere dynamics and chemistry. *J Geophys Res* 99:3759–3776. <https://doi.org/10.1029/93JE03431>
- Bougher SW, Brain DA, Fox JL et al (2017) Upper neutral atmosphere and ionosphere. In: Haberle RM, Clancy RT, Forget F et al (eds) *The atmosphere and climate of Mars*, pp 405–432. <https://doi.org/10.1017/9781139060172.014>
- Brain DA, Halekas JS, Peticolas LM et al (2006) On the origin of aurorae on Mars. *Geophys Res Lett* 33:L01201. <https://doi.org/10.1029/2005GL024782>
- Brain DA, Lillis RJ, Mitchell DL et al (2007) Electron pitch angle distributions as indicators of magnetic field topology near Mars. *J Geophys Res Space Phys* 112:A09201. <https://doi.org/10.1029/2007JA012435>
- Chaffin MS, Chaufray JY, Stewart I et al (2014) Unexpected variability of Martian hydrogen escape. *Geophys Res Lett* 41:314–320. <https://doi.org/10.1002/2013GL058578>
- Chaffin MS, Deighan J, Schneider NM et al (2017) Elevated atmospheric escape of atomic hydrogen from Mars induced by high-altitude water. *Nat Geophys* 10:174–178. <https://doi.org/10.1038/ngeo2887>
- Chaffin MS, Chaufray JY, Deighan J et al (2018) Mars H escape rates derived from MAVEN/IUVS Lyman Alpha brightness measurements and their dependence on model assumptions. *J Geophys Res, Planets* 123:2192–2210. <https://doi.org/10.1029/2018JE005574>
- Chaffin MS, Deighan J, Jain S et al (2022a) Combined analysis of hydrogen and oxygen 102.6 nm emission at Mars. *Geophys Res Lett* 49(16):e99851. <https://doi.org/10.1029/2022GL099851>
- Chaffin MS, Fowler CM, Deighan J et al (2022b) Patchy proton aurora at Mars: a global view of solar wind precipitation across the Martian dayside from EMM/EMUS. *Geophys Res Lett* 49:e99881. <https://doi.org/10.1029/2022GL099881>
- Chamberlain JW (1963) Planetary coronae and atmospheric evaporation. *Planet Space Sci* 11:901–960. [https://doi.org/10.1016/0032-0633\(63\)90122-3](https://doi.org/10.1016/0032-0633(63)90122-3)
- Chassefière E, Leblanc F (2004) Mars atmospheric escape and evolution: interaction with the solar wind. *Planet Space Sci* 52:1039–1058. <https://doi.org/10.1026/j.pss.2004.07.002>

- Chaufray JY, Modolo R, Leblanc F et al (2007) Mars solar wind interaction: formation of the Martian corona and atmospheric loss to space. *J Geophys Res* 112:e09009. <https://doi.org/10.1029/2007JE002915>
- Chaufray JY, Bertaux JL, Leblanc F et al (2008) Observation of the hydrogen corona with SPICAM on Mars Express. *Icarus* 76:598–613. <https://doi.org/10.1016/j.icarus.2008.01.009>
- Chaufray JY, Leblanc F, Quémerais E et al (2009) Martian oxygen density at the exobase deduced from O I 130.4-nm observations by spectroscopy for the investigation of the characteristics of the atmosphere of Mars on Mars Express. *J Geophys Res, Planets* 114(E2):E02006. <https://doi.org/10.1029/2008JE003130>
- Chaufray JY, Gonzalez-Galindo F, Forget F et al (2015) Variability of the hydrogen in the Martian upper atmosphere as simulated with a 3D atmosphere-exosphere coupling. *Icarus* 245:282–294. <https://doi.org/10.1016/j.icarus.2014.08.38>
- Chaufray JY, Gonzalez-Galindo F, Lopez-Valverde M et al (2021a) Study of the hydrogen escape rate at Mars during Martian years 28 and 29 from comparisons between SPICAM/Mars Express observations and GCM-LMD simulations. *Icarus* 353:113498. <https://doi.org/10.1016/j.icarus.2019.113498>
- Chaufray JY, Mayyasi M, Chaffin M et al (2021b) Estimate of the D/H ratio in the Martian upper atmosphere from the low spectral resolution mode of MAVEN/IUVS. *J Geophys Res, Planets* 126:e06814. <https://doi.org/10.1029/2020JE006814>
- Clancy RT, Sandor BJ, Wolff MJ et al (2012) Extensive MRO CRISM observations of 1.27  $\mu\text{m}$  O<sub>2</sub> airglow in Mars polar night and their comparison to MRO MCS temperature profiles and LMD GCM simulations. *J Geophys Res, Planets* 117:E00J10. <https://doi.org/10.1029/2011JE004018>
- Clarke JT, Bertaux JL, Chaufray JY et al (2014) A rapid decrease of the hydrogen corona of Mars. *Geophys Res Lett* 41:8013–8020. <https://doi.org/10.1002/2014GL061803>
- Clarke J, Mayyasi M, Bhattacharyya SND et al (2017) Variability of D and H in the Martian upper atmosphere observed with MAVEN IUVS echelle channel. *J Geophys Res* 122:2336–2344. <https://doi.org/10.1002/2016JA023479>
- Cox C, Saglam A, Gérard JC et al (2008) Distribution of the ultraviolet nitric oxide Martian night airglow: observations from Mars Express and comparisons with a one-dimensional model. *J Geophys Res, Planets* 113(E8):E08012. <https://doi.org/10.1029/2007JE003037>
- Cox C, Gérard JC, Hubert B et al (2010) Mars ultraviolet dayglow variability: SPICAM observations and comparison with airglow model. *J Geophys Res, Planets* 115(E4):E04010. <https://doi.org/10.1029/2009JE003504>
- Deighan J, Chaffin MS, Chaufray JY et al (2015) Maven iuvsv observation of the hot corona at Mars. *Geophys Res Lett* 42:9009–9014. <https://doi.org/10.1002/2015GL065487>
- Deighan J, Jain SK, Chaffin MS et al (2018) Discovery of a proton aurora at Mars. *Nat Astron* 2:802–807. <https://doi.org/10.1038/s41550-018-0538-5>
- Deming D, Espenak F, Jennings D et al (1983) Observations of the 10-  $\mu\text{m}$  natural laser emission from the mesospheres of Mars and Venus. *Icarus* 55(3):347–355. [https://doi.org/10.1016/0019-1035\(83\)90107-0](https://doi.org/10.1016/0019-1035(83)90107-0)
- Fang X, Ma Y, Schneider N et al (2022) Discrete aurora on the nightside of Mars: occurrence location and probability. *J Geophys Res Space Phys* 127:e29716. <https://doi.org/10.1029/2021JA029716>
- Fedorova A, Korabiev O, Perrier S et al (2006) Observation of O<sub>2</sub> 1.27  $\mu\text{m}$  dayglow by SPICAM IR: seasonal distribution for the first Martian year of Mars Express. *J Geophys Res, Planets* 111:E09S07. <https://doi.org/10.1029/2006JE002694>
- Fedorova AA, Lefèvre F, Guslyakova S et al (2012) The O<sub>2</sub> nightglow in the Martian atmosphere by SPICAM onboard of Mars-Express. *Icarus* 219:596–608. <https://doi.org/10.1016/j.icarus.2012.03.031>
- Forget F, Hourdin F, Fournier R et al (1999) Improved general circulation models of the Martian atmosphere from the surface to above 80 km. *J Geophys Res* 104:24155–24175. <https://doi.org/10.1029/1999JE001025>
- Forget F, Montmessin F, Bertaux JL et al (2009) Density and temperatures of the upper Martian atmosphere measured by stellar occultations with Mars Express SPICAM. *J Geophys Res, Planets* 114:E01004. <https://doi.org/10.1029/2008JE003086>
- Formisano V, Angrilli F, Arnold G et al (2005a) The Planetary Fourier Spectrometer (PFS) onboard the European Mars Express mission. *Planet Space Sci* 53:963–974. <https://doi.org/10.1016/j.pss.2004.12.006>
- Formisano V, Encenaz T, Fonti S et al (2005b) A Martian PFS average spectrum: comparison with ISO SWS. *Planet Space Sci* 53:1043–1052. <https://doi.org/10.1016/j.pss.2005.03.009>
- Formisano V, Maturilli A, Giuranna M et al (2006) Observations of non-LTE emission at 4.5 microns with the planetary Fourier spectrometer aboard the Mars Express mission. *Icarus* 182:51–67. <https://doi.org/10.1016/j.icarus.2005.12.022>
- Fox JL (1992) Airglow and aurora in the atmospheres of Venus and Mars. Washington DC Am Geophys Union Geophys Monograph Ser 66:191–222. <https://doi.org/10.1029/GM066p0191>

- Fox JL, Dalgarno A (1979) Ionization, luminosity, and heating of the upper atmosphere of Mars. *J Geophys Res* 84:7315–7333. <https://doi.org/10.1029/JA084iA12p07315>
- Fox JL, Hać NEF (2013) Intensities of the Martian N<sub>2</sub> electron-impact excited dayglow emissions. *Geophys Res Lett* 40:2529–2533. <https://doi.org/10.1002/grl.50435>
- Gagné ME, Bertaux JL, González-Galindo F et al (2013) New nitric oxide (NO) nightglow measurements with SPICAM/MEX as a tracer of Mars upper atmosphere circulation and comparison with LMD-MGCM model prediction: evidence for asymmetric hemispheres. *J Geophys Res, Planets* 118(10):2172–2179. <https://doi.org/10.1002/jgre.20165>
- García Muñoz A, McConnell JC, McDade IC et al (2005) Airglow on Mars: some model expectations for the OH Meinel bands and the O<sub>2</sub> IR atmospheric band. *Icarus* 176:75–95. <https://doi.org/10.1016/j.icarus.2005.01.006>
- Gérard JC, Hubert B, Shematovich VI et al (2008a) The Venus ultraviolet oxygen dayglow and aurora: model comparison with observations. *Planet Space Sci* 56:542–552. <https://doi.org/10.1016/j.pss.2007.11.008>
- Gérard JC, Saglam A, Piccioni G et al (2008b) Distribution of the O<sub>2</sub> infrared nightglow observed with VIR-TIS on board Venus Express. *Geophys Res Lett* 35:L02207. <https://doi.org/10.1029/2007GL032021>
- Gérard JC, Soret L, Libert L et al (2015) Concurrent observations of ultraviolet aurora and energetic electron precipitation with Mars Express. *J Geophys Res Space Phys* 120:6749–6765. <https://doi.org/10.1002/2015JA021150>
- Gérard JC, Hubert B, Ritter B et al (2019) Lyman- $\alpha$  emission in the Martian proton aurora: line profile and role of horizontal induced magnetic field. *Icarus* 321:266–271. <https://doi.org/10.1016/j.icarus.2018.11.013>
- Gérard JC, Aoki S, Willame Y et al (2020) Detection of green line emission in the dayside atmosphere of Mars from NOMAD-TGO observations. *Nat Astron* 4:1049–1052. <https://doi.org/10.1038/s41550-020-1123-2>
- Gérard JC, Aoki S, Gkouvelis L et al (2021) First observation of the oxygen 630 nm emission in the Martian dayglow. *Geophys Res Lett* 48(8):e92334. <https://doi.org/10.1029/2020GL092334>
- Gérard JC, Soret L, Thomas IR et al (2023) Observation of the Mars O<sub>2</sub> visible nightglow by the NOMAD spectrometer onboard the Trace Gas Orbiter. *Nat Astron* 8:77–81. <https://doi.org/10.1038/s41550-023-02104-8>
- Girazian Z, Schneider NM, Milby Z et al (2022) Discrete aurora at Mars: dependence on upstream solar wind conditions. *J Geophys Res Space Phys* 127:e30238. <https://doi.org/10.1029/2021JA030238>
- Giuranna M, Fonte S, Longobardo A et al (2018) PFS/MEX limb observations of 4.3- $\mu$ m CO<sub>2</sub> non-LTE emission in the atmosphere of Mars. *Icarus* 315:46–60. <https://doi.org/10.1016/j.icarus.2018.06.018>
- Giuranna M, Tellmann S, Montmessin F et al (2024) Vertical structure of the Martian atmosphere: the view from Mars Express. *Space Sci Rev* 220
- Gkouvelis L, Gérard JC, Ritter B et al (2018) The O(<sup>1</sup>S) 297.2-nm dayglow emission: a tracer of CO<sub>2</sub> density variations in the Martian lower thermosphere. *J Geophys Res, Planets* 123(12):3119–3132. <https://doi.org/10.1029/2018JE005709>
- Gkouvelis L, Gérard JC, Ritter B et al (2020) Airglow remote sensing of the seasonal variation of the Martian upper atmosphere: MAVEN limb observations and model comparison. *Icarus* 341:113666. <https://doi.org/10.1016/j.icarus.2020.113666>
- González-Galindo F, Forget F, Lopez-Valverde MA et al (2009) A ground-to-exosphere Martian general circulation model: 1 seasonal, diurnal, and solar cycle variation of thermospheric temperatures. *J Geophys Res* 114:E04001. <https://doi.org/10.1029/2008JE003246>
- González-Galindo F, Chaufray JY, Forget F et al (2018) UV dayglow variability on Mars: simulation with a global climate model and comparison with SPICAM/MEX data. *J Geophys Res, Planets* 123(7):1934–1952. <https://doi.org/10.1029/2018JE005556>
- González-Galindo F, Jiménez-Monferrer S, López-Valverde MÁ et al (2021) On the derivation of thermospheric temperatures from dayglow emissions on Mars. *Icarus* 358:114284. <https://doi.org/10.1016/j.icarus.2020.114284>
- Gorinov DA, Khatuntsev IV, Zasova LV et al (2018) Circulation of Venusian atmosphere at 90–110 km based on apparent motions of the O<sub>2</sub> 1.27  $\mu$ m nightglow from VIRTIS-M (Venus Express) data. *Geophys Res Lett* 45:2554–2562. <https://doi.org/10.1002/2017GL076380>
- Guslyakova S, Fedorova A, Lefèvre F et al (2016) Long-term nadir observations of the O<sub>2</sub> dayglow by SPICAM IR. *Planet Space Sci* 122:1–12. <https://doi.org/10.1016/j.pss.2015.12.006>
- Holsclaw GM, Deighan J, Almatroushi H et al (2021) The Emirates Mars Ultraviolet Spectrometer (EMUS) for the EMM mission. *Space Sci Rev* 217(8):79. <https://doi.org/10.1007/s11214-021-00854-3>
- Hughes A, Chaffin M, Mierkiewicz E et al (2019) Proton aurora on Mars: a dayside phenomenon pervasive in southern summer. *J Geophys Res Space Phys* 124:10533–10548. <https://doi.org/10.1029/2019JA027140>


- Jain SK, Bhardwaj A (2011) Model calculation of N<sub>2</sub> Vegard-Kaplan band emissions in Martian dayglow. *J Geophys Res, Planets* 116:E07005. <https://doi.org/10.1029/2010JE003778>
- Jain SK, Bhardwaj A (2012) Impact of solar EUV flux on CO Cameron band and CO<sub>2</sub><sup>+</sup> UV doublet emissions in the dayglow of Mars. *Planet Space Sci* 63:110–122. <https://doi.org/10.1016/j.pss.2011.08.010>
- Jain SK, Deighan J, Schneider NM et al (2018) Martian thermospheric response to an X8.2 solar flare on 10 September 2017 as seen by MAVEN/IUVS. *Geophys Res Lett* 45:7312–7319. <https://doi.org/10.1029/2018GL077731>
- Jain SK, Bougher SW, Deighan J et al (2020) Martian thermospheric warming associated with the planet encircling dust event of 2018. *Geophys Res Lett* 47:e85302. <https://doi.org/10.1029/2019GL085302>
- Jain SK, Deighan J, Chaffin M et al (2022) Morphology of extreme and far ultraviolet Martian airglow emissions observed by the EMUS instrument on board the Emirates Mars Mission. *Geophys Res Lett* 49:e2022GL099885. <https://doi.org/10.1029/2022GL099885>
- Jain SK, Soto E, Evans JS et al (2023) Thermal structure of Mars' middle and upper atmospheres: understanding the impacts of dynamics and solar forcing. *Icarus* 393:114703. <https://doi.org/10.1016/j.icarus.2021.114703>
- Jakosky BM, Lin RP, Grebowsky JM et al (2015) The Mars Atmosphere and Volatile Evolution (MAVEN) mission. *Space Sci Rev* 195:3–48. <https://doi.org/10.1007/s11214-015-0139-x>
- Jiménez-Monferrer S, López-Valverde MA, Funke B et al (2021) CO<sub>2</sub> retrievals in the Mars daylight thermosphere from its 4.3 μm limb emission measured by OMEGA/MEx. *Icarus* 353:113830. <https://doi.org/10.1016/j.icarus.2020.113830>
- Johnson RE, Combi MR, Fox JL et al (2008) Exospheres and atmospheric escape. *Space Sci Rev* 139:355–397. <https://doi.org/10.1007/s11214-008-9415-3>
- Krasnopolsky VA (1997) Photochemical mapping of Mars. *J Geophys Res* 102:13313–13320. <https://doi.org/10.1029/97JE01085>
- Krasnopolsky VA (2003) Mapping of Mars O<sub>2</sub> 1.27 μm dayglow at four seasonal points. *Icarus* 165(2):315–325. [https://doi.org/10.1016/S0019-1035\(03\)00214-8](https://doi.org/10.1016/S0019-1035(03)00214-8)
- Krasnopolsky VA (2007) Long-term spectroscopic observations of Mars using IRTF/CSHELL: mapping of O<sub>2</sub> dayglow, CO, and search for CH<sub>4</sub>. *Icarus* 190:93–102. <https://doi.org/10.1016/j.icarus.2007.02.014>
- Krasnopolsky VA (2013) Night and day airglow of oxygen at 1.27 μm on Mars. *Planet Space Sci* 85:243–249. <https://doi.org/10.1016/j.pss.2013.06.018>
- Krasnopolsky VA, Feldman PD (2002) Far ultraviolet spectrum of Mars. *Icarus* 160(1):86–94. <https://doi.org/10.1006/icar.2002.6949>
- Krasnopolsky VA, Mumma MJ, Randall Gladstone G (1998) Detection of atomic deuterium in the upper atmosphere of Mars. *Science* 280:1576. <https://doi.org/10.1126/science.280.5369.1576>
- Leblanc F, Chaufray JY, Liliensten J et al (2006a) Martian dayglow as seen by the SPICAM UV spectrograph on Mars Express. *J Geophys Res, Planets* 111(E9):E09S11. <https://doi.org/10.1029/2005JE002664>
- Leblanc F, Witasse O, Winningham J et al (2006b) Origins of the Martian aurora observed by Spectroscopy for Investigation of Characteristics of the Atmosphere of Mars (SPICAM) on board Mars Express. *J Geophys Res Space Phys* 111:A09313. <https://doi.org/10.1029/2006JA011763>
- Leblanc F, Chaufray JY, Bertaux JL (2007) On Martian nitrogen dayglow emission observed by SPICAM UV spectrograph/Mars Express. *Geophys Res Lett* 34:L02206. <https://doi.org/10.1029/2006GL028437>
- Leblanc F, Witasse O, Liliensten J et al (2008) Observations of aurorae by SPICAM ultraviolet spectrograph on board Mars Express: simultaneous ASPERA-3 and MARSIS measurements. *J Geophys Res Space Phys* 113:A08311. <https://doi.org/10.1029/2008JA013033>
- Lee RA, Ajello JM, Malone CP et al (2021) Laboratory study of the Cameron bands, the first negative bands, and fourth positive bands in the middle ultraviolet 180–280 nm by electron impact upon CO. *J Geophys Res, Planets* 126(1):e06602. <https://doi.org/10.1029/2020JE006602>
- Lee RA, Ajello JM, Malone CP et al (2022) Laboratory study of the Cameron bands and UV doublet in the middle ultraviolet 180–300 nm by electron impact upon CO<sub>2</sub> with application to Mars. *Astrophys J* 938(2):99. <https://doi.org/10.3847/1538-4357/ac88c8>
- Lefèvre F, Lebonnois S, Montmessin F et al (2004) Three-dimensional modeling of ozone on Mars. *J Geophys Res, Planets* 109:E07004. <https://doi.org/10.1029/2004JE002268>
- Lefèvre F, Bertaux JL, Clancy RT et al (2008) Heterogeneous chemistry in the atmosphere of Mars. *Nature* 454:971–975. <https://doi.org/10.1038/nature07116>
- Lellouch E, Encrenaz T, de Graauw T et al (2000) The 2.4–45 μm spectrum of Mars observed with the infrared space observatory. *Planet Space Sci* 48:1393–1405. [https://doi.org/10.1016/S0032-0633\(00\)00118-5](https://doi.org/10.1016/S0032-0633(00)00118-5)
- Lillis RJ, Deighan J, Brain D et al (2022) First synoptic images of FUV discrete aurora and discovery of sinuous aurora at Mars by EMM EMUS. *Geophys Res Lett* 49:e99820. <https://doi.org/10.1029/2022GL099820>
- Lo DY, Yelle RV, Deighan JI et al (2022) MAVEN/IUVS observations of C I 156.1 nm and 165.7 nm dayglow: direct detection of carbon and implications on photochemical escape. *Icarus* 371:114664. <https://doi.org/10.1016/j.icarus.2021.114664>

- López-Puertas M, Taylor FW (2001) Non-LTE radiative transfer in the atmosphere. World Scientific, Singapore. <https://doi.org/10.1142/4650>
- López-Valverde MA, López-Puertas M, López-Moreno JJ et al (2005) Analysis of CO<sub>2</sub> non-LTE emissions at 4.3 μm in the Martian atmosphere as observed by PFS/Mars Express and SWS/ISO. *Planet Space Sci* 53:1079–1087. <https://doi.org/10.1016/j.pss.2005.03.007>
- López-Valverde MA, López-Puertas M, Funke B et al (2011) Modeling the atmospheric limb emission of CO<sub>2</sub> at 4.3 μm in the terrestrial planets. *Planet Space Sci* 59:988–998. <https://doi.org/10.1016/j.pss.2010.02.001>
- Lundin R, Winningham D, Barabash S et al (2006a) Plasma acceleration above Martian magnetic anomalies. *Science* 311:980–983. <https://doi.org/10.1126/science.1122071>
- Lundin R, Winningham D, Barabash S et al (2006b) Ionospheric plasma acceleration at Mars: ASPERA-3 results. *Icarus* 182:308–319. <https://doi.org/10.1016/j.icarus.2005.10.035>
- Maltagliati L, Montmessin F, Korabev O et al (2013) Annual survey of water vapor vertical distribution and water: aerosol coupling in the Martian atmosphere observed by SPICAM/Mex solar occultations. *Icarus* 223:942–962. <https://doi.org/10.1016/j.icarus.2012.12.012>
- Mayyasi M, Clarke J, Bhattacharyya D et al (2017) The variability of atmospheric deuterium brightness at Mars: evidence for seasonal dependence. *J Geophys Res Space Phys* 122:10811–10823. <https://doi.org/10.1002/2017JA024666>
- Mayyasi M, Clarke J, Chaufray JY et al (2023) Solar cycle and seasonal variability of H in the upper atmosphere of Mars. *Icarus* 393:115293. <https://doi.org/10.1016/j.icarus.2022.115293>
- McClintock WE, Schneider NM, Holsclaw GM et al (2015) The Imaging Ultraviolet Spectrograph (IUVS) for the MAVEN mission. *Space Sci Rev* 195:75–124. <https://doi.org/10.1007/s11214-014-0098-7>
- McElroy MB (1972) Mars: an evolving atmosphere. *Science* 175:443–445. <https://doi.org/10.1126/science.175.4020.443>
- Medvedev AS, González-Galindo F, Yiğit E et al (2015) Cooling of the Martian thermosphere by CO<sub>2</sub> radiation and gravity waves: an intercomparison study with two general circulation models. *J Geophys Res, Planets* 120:913–927. <https://doi.org/10.1002/2015JE004802>
- Mitchell DL, Lin RP, Mazelle C et al (2001) Probing Mars' crustal magnetic field and ionosphere with the MGS Electron Reflectometer. *J Geophys Res* 106:23419–23428. <https://doi.org/10.1029/2000JE001435>
- Montmessin F, Korabev O, Lefèvre F et al (2017) SPICAM on Mars Express: a 10 year in-depth survey of the Martian atmosphere. *Icarus* 297:195–216. <https://doi.org/10.1016/j.icarus.2017.06.022>
- Montmessin F, Fedorova A, Alday J et al (2024) Mars' water cycle and escape: a view from Mars Express and beyond. *Space Sci Rev* 220
- Noxon JF, Traub WA, Carleton NP et al (1976) Detection of O<sub>2</sub> dayglow emission from Mars and the Martian ozone abundance. *Astrophys J* 207:1025–1035. <https://doi.org/10.1086/154572>
- Perrier S, Bertaux JL, Lefèvre F et al (2006) Global distribution of total ozone on Mars from SPICAM/MEX UV measurements. *J Geophys Res, Planets* 111:E09S06. <https://doi.org/10.1029/2006JE002681>
- Peter K, Sánchez-Cano B, Nemeč F et al (2024) The ionosphere of Mars after 20 years of Mars Express contributions. *Space Sci Rev* 220
- Piccialli A, López-Valverde MA, Määttänen A et al (2016) CO<sub>2</sub> non-LTE limb emissions in Mars' atmosphere as observed by OMEGA/Mars Express. *J Geophys Res, Planets* 121:1066–1086. <https://doi.org/10.1002/2015JE004981>
- Ritter B, Gérard JC, Hubert B et al (2018) Observations of the proton aurora on Mars with SPICAM on board Mars Express. *Geophys Res Lett* 45:612–619. <https://doi.org/10.1002/2017GL076235>
- Safaieinili A, Kofman W, Mouginot J et al (2007) Estimation of the total electron content of the Martian ionosphere using radar sounder surface echoes. *Geophys Res Lett* 34:L23204. <https://doi.org/10.1029/2007GL032154>
- Sanchez-Cano B, Opgenoorth H, Leblanc F et al (2022) The M-MATISSE mission: Mars Magnetosphere Atmosphere Ionosphere and Surface Science. In: 44th COSPAR scientific assembly. Held 16–24 July, p 421
- Schneider NM, Deighan JI, Jain SK et al (2015) Discovery of diffuse aurora on Mars. *Science* 350:0313. <https://doi.org/10.1126/science.aad0313>
- Schneider NM, Jain SK, Deighan J et al (2018) Global aurora on Mars during the September 2017 space weather event. *Geophys Res Lett* 45:7391–7398. <https://doi.org/10.1029/2018GL077772>
- Schneider NM, Milby Z, Jain SK et al (2020) Imaging of Martian circulation patterns and atmospheric tides through MAVEN/IUVS nightglow observations. *J Geophys Res Space Phys* 125:e27318. <https://doi.org/10.1029/2019JA027318>
- Schneider NM, Milby Z, Jain SK et al (2021) Discrete aurora on Mars: insights into their distribution and activity from MAVEN/IUVS observations. *J Geophys Res Space Phys* 126:e29428. <https://doi.org/10.1029/2021JA029428>

- Shematovich VI, Bisikalo DV, Gérard JC et al (2008) Monte Carlo model of electron transport for the calculation of Mars dayglow emissions. *J Geophys Res, Planets* 113(E2):E02011. <https://doi.org/10.1029/2007JE002938>
- Soret L, Gérard JC, Libert L et al (2016) SPICAM observations and modeling of Mars aurorae. *Icarus* 264:398–406. <https://doi.org/10.1016/j.icarus.2015.09.023>
- Soret L, Gérard JC, Schneider N et al (2021) Discrete aurora on Mars: spectral properties, vertical profiles, and electron energies. *J Geophys Res Space Phys* 126(10):e29495. <https://doi.org/10.1029/2021JA029495>
- Soret L, Gérard JC, Aoki S et al (2022) The Mars oxygen visible dayglow: a Martian year of NOMAD/UVIS observations. *J Geophys Res, Planets* 127(6):e07220. <https://doi.org/10.1029/2022JE007220>
- Soret L, Gérard JC, Hubert B et al (2023) The ultraviolet Martian dayglow observed with NOMAD/UVIS on ExoMars Trace Gas Orbiter. *J Geophys Res, Planets* 128:e2023JE007762. <https://doi.org/10.1029/2023JE007762>
- Stevens MH, Evans JS, Schneider NM et al (2015) New observations of molecular nitrogen in the Martian upper atmosphere by IUVS on MAVEN. *Geophys Res Lett* 42:9050–9056. <https://doi.org/10.1002/2015GL065319>
- Stevens MH, Siskind DE, Evans JS et al (2019) Detection of the nitric oxide dayglow on Mars by MAVEN/IUVS. *J Geophys Res, Planets* 124:1226–1237. <https://doi.org/10.1029/2019JE005945>
- Stewart AI, Barth CA, Hord CW et al (1972) Mariner 9 ultraviolet spectrometer experiment: structure of Mars's upper atmosphere (A 5.3). *Icarus* 17(2):469–474. [https://doi.org/10.1016/0019-1035\(72\)90012-7](https://doi.org/10.1016/0019-1035(72)90012-7)
- Stiepen A, Gérard JC, Bougher S et al (2015a) Mars thermospheric scale height: CO Cameron and CO<sub>2</sub><sup>+</sup> dayglow observations from Mars Express. *Icarus* 245:295–305. <https://doi.org/10.1016/j.icarus.2014.09.051>
- Stiepen A, Gérard JC, Gagné MÉ et al (2015b) Ten years of Martian nitric oxide nightglow observations. *Geophys Res Lett* 42(3):720–725. <https://doi.org/10.1002/2014GL062300>
- Stiepen A, Jain SK, Schneider NM et al (2017) Nitric oxide nightglow and Martian mesospheric circulation from MAVEN/IUVS observations and LMD-MGCM predictions. *J Geophys Res Space Phys* 122:5782–5797. <https://doi.org/10.1002/2016JA023523>
- Strickland DJ, Stewart AI, Barth CA et al (1973) Mariner 9 ultraviolet spectrometer experiment: Mars atomic oxygen 1304-Å emission. *J Geophys Res* 78(22):4547. <https://doi.org/10.1029/JA078i022p04547>
- Vandaele AC, Aoki S, Bauduin S et al (2024) Composition and chemistry of the Martian atmosphere. *Space Sci Rev* 220
- Widemann T, Ghail RC, Wilson CF et al (2022) The envision mission to Venus. In: 53rd Lunar and Planetary Science Conference, p 2948
- Wilson C, Titov D, Holmström M et al (2024) Mars Express scientific payload and its evolution. *Space Sci Rev*, 220
- Xu S, Mitchell DL, McFadden JP et al (2022) Nightside auroral electrons at Mars: upstream drivers and ionospheric impact. *J Geophys Res Space Phys* 127:e30801. <https://doi.org/10.1029/2022JA030801>

**Publisher's Note** Springer Nature remains neutral with regard to jurisdictional claims in published maps and institutional affiliations.

## Authors and Affiliations

Francisco González-Galindo<sup>1</sup>  · Jean-Claude Gérard<sup>2</sup> · Lauriane Soret<sup>2</sup> · Jean-Yves Chaufray<sup>3</sup> · Anna Fedorova<sup>4</sup> · Mats Holmstrom<sup>5</sup> · Franck Lefèvre<sup>3</sup> · Miguel Ángel López-Valverde<sup>1</sup> · Franck Montmessin<sup>3</sup>

✉ F. González-Galindo  
[ggalindo@iaa.es](mailto:ggalindo@iaa.es)

J.-C. Gérard  
[JC.Gerard@uliege.be](mailto:JC.Gerard@uliege.be)

L. Soret  
[lauriane.soret@uliege.be](mailto:lauriane.soret@uliege.be)

J.-Y. Chaufray  
[Jean-Yves.Chaufray@latmos.ipsl.fr](mailto:Jean-Yves.Chaufray@latmos.ipsl.fr)

A. Fedorova  
[fedorova@iki.rssi.ru](mailto:fedorova@iki.rssi.ru)

M. Holmstrom  
[matsh@irf.se](mailto:matsh@irf.se)

F. Lefèvre  
[franck.lefevre@latmos.ipsl.fr](mailto:franck.lefevre@latmos.ipsl.fr)

M.Á. López-Valverde  
[valverde@iaa.es](mailto:valverde@iaa.es)

F. Montmessin  
[Franck.Montmessin@latmos.ipsl.fr](mailto:Franck.Montmessin@latmos.ipsl.fr)

- <sup>1</sup> Instituto de Astrofísica de Andalucía, CSIC, Glorieta de la Astronomía, Granada, Spain
- <sup>2</sup> LPAP, STAR Institute, Université de Liège, Liège, Belgium
- <sup>3</sup> LATMOS, IPSL, Paris, France
- <sup>4</sup> IKI, Moscow, Russia
- <sup>5</sup> Swedish Institute of Space Physics, Kiruna, Sweden